R-13-53

Long term stability of rock caverns BMA and BLA of SFR, Forsmark

Diego Mas Ivars, María Veiga Ríos
Itasca Consultants AB

Wenjie Shiu, Itasca Consultants SAS

Fredrik Johansson, Anders Fredriksson
Sweco Infrastructure AB

December 2014

Svensk Kärnbränslehantering AB
Swedish Nuclear Fuel
and Waste Management Co

Box 250, SE-101 24 Stockholm
Phone +46 8 459 84 00

ISSN 1402-3091
SKB R-13-53
ID 1339566

Long term stability of rock caverns BMA and BLA of SFR, Forsmark

Diego Mas Ivars, María Veiga Ríos
Itasca Consultants AB

Wenjie Shiu, Itasca Consultants SAS

Fredrik Johansson, Anders Fredriksson
Sweco Infrastructure AB

December 2014

Abstract

This report describes a study of long term stability of the caverns BMA and BLA in SFR1. The stability was analyzed using the three dimensional numerical code 3DEC (Itasca 2011). The study was limited to 100 m along the two largest caverns within an area with two minor deformation zones. These deformation zones are oriented with a strike in a large angle to the caverns, and with a plunge such that they have the potential to form a large wedge above the caverns. A random fracture generator has been used to construct 3DEC models that capture the statistics of the mapped fractures at the studied caverns at SFR. BLA was modelled as being empty, while BMA was modelled assuming that the void between the concrete structure and the rock was backfilled with sand.

In the calculations, different models of the rock mass with respect to fracture orientations was analyzed. Analyzes was done assuming both deformable and rigid block in the rock mass. In order to model the degradation of the rock mass adjacent to the cavern walls, the strength of the fractures in the rock mass has been successively reduced in the numerical calculations. With this methodology an assumed loosening process is modelled. A number of conservative assumptions was made; fractures has infinite length, the fracture shear dilation angle was set to zero degrees and the uncertainty in in situ stress magnitudes has been considered.

The caverns and the pillar between them remain stable in the numerical analyses without rock reinforcement with the assumed fracture properties and the modelled gradual reduction of the fracture properties. At low friction angles, blocks can start to fall into the caverns. In one simulated case, the loosening of the rock mass reaches a height of up to 34 m above the cavern roof. At this stage, the deformation at the rock surface is about 3.5 cm. But still the pillar between the caverns was intact. However, it should be emphasized that the friction angle required to make this happen is unrealistically low.

Contents

1 Introduction

1.1 Background

On behalf of SKB, Sweco Infrastructure AB and Itasca Consultants AB have conducted a numerical analysis of the long term stability of the rock caverns for the final repository of low and intermediate level active nuclear waste. The most recent safety assessment for SFR is described in SKB (2014) where a time span of 100,000 years is applied. This investigation is based on earlier safety assessments for SFR which considered a time span of 10,000 years (SKB 2001, 2008).

Rock strength changes around the rock caverns may result in rock block fallout if there is no proper backfill in the caverns. Such rock fallout would affect the dimensions, geometry and properties of the concrete structures in such a cavern. Changes in the rock around the rock caverns also cause changes in the size and direction of the water flow which will also affect radionuclide transport (SKB 2008).

A separate study has evaluated the possibilities of rock fallout in the rock caverns (SKBdoc 1237025). The analysis was essentially qualitative and assessed the maximum rock fallout possible. In an empty rock cavern the loosening proceeds until the cavern has been completely filled with fallen rock so that a support is exerted against the remaining rock. The rock volume that is loosened and falls into the rock cavern increase in volume by about 40 percent. A pessimistic estimate of the maximum size of the loose zone was about 10 meters (SKBdoc 1237025). No top filling in the caverns was assumed.

The objective of this report is to analyze if there exists a long term risk for an ongoing loosening of the rock mass due to degradation and weathering of the rock mass adjacent to the walls of the rock caverns. An additional objective is to analyze if the long term stability of the pillar between the repository rooms is affected.

In order to analyze the stability, three dimensional numerical analyses have been performed with the program 3DEC (version 3DEC dp 4.20.123 64 bit; Itasca 2011). In the calculations, different models of the rock mass with respect to fracture orientations have been analyzed. In order to model the degradation of the rock mass adjacent to the cavern walls, the strength of the fractures in the rock mass has been successively reduced in the numerical calculations. With this methodology the loosening process is modeled. The final results show if loosening of the rock mass progresses to the surface of the rock, or if the cavern will be filled with blocks, and therefore be self-supporting, before this occurs. The results also show if the long term stability of the pillar between the rooms is affected.

In this report, the layout of the SRF and a description of the analyzed repository rooms are first illustrated. After that, input data to the calculations are presented. This is followed by a description of the methodology of the calculations. Thereafter, analyses of the results are presented and a summary together with conclusions are presented.

1.2 Layout of the SFR

The layout in this study includes only the existing SFR (SFR 1) i.e. the extention of the facility is not considered. SFR consists of four horizontal repository rooms and one vertical repository silo together with access and construction tunnel, see Figure 1-1. The repository rooms are situated in rock beneath the sea floor, covered by about 60 meters of rock. The four horizontal repository rooms are called: BMA, BLA, 1 BTF and 2 BTF . In each end of the rooms a loading and transshipment zone exits. Between the loading and transshipment zones and the surrounding tunnel system, short access tunnels exists where plugs will be constructed in order to seal the SFR. In Figure 1-2 a section through the repository rooms is presented.

1.2.1 Plugs

Plugs will be constructed in the access tunnels to the repository rooms in order to seal them, see Figure 1-1.

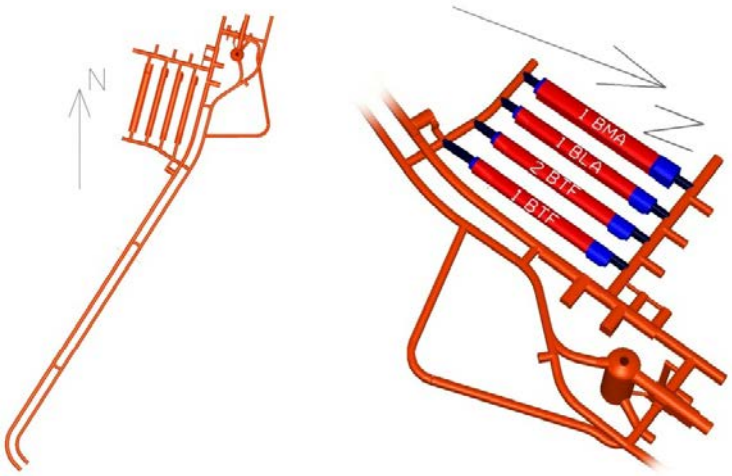

Figure 1-1. *To the left: Entire system of tunnnels and rooms in SFR. To the right: Red repository rooms with blue loading and transhipment zones and black plugs.*

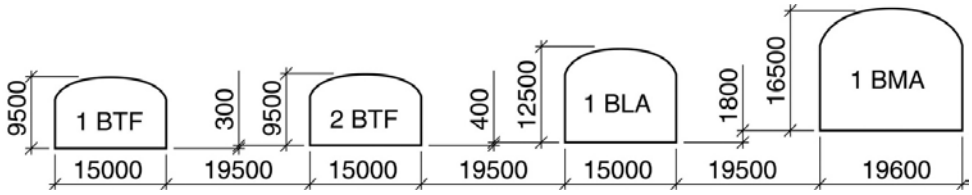

Figure 1-2. *Section through the repository rooms.*

1.2.2 Repository room 1 BTF and 2 BTF

The geometry of repository rooms 1 BFT and 2 BFT can be seen in Figure 1-3. In general the geometries of 1 BFT and 2 BFT are identical.

Type of waste and backfill

In 1 BTF and 2 BTF the waste is low-level. In 1 BTF, the waste is contained in barrels which are stacked within the concrete tanks. The barrels are successively cast in concrete of low viscosity. The waste in 2 BTF consists of concrete tanks stacked on each other. The spaces between the tanks are also filled with concrete of low viscosity when the rooms are sealed.

On top of the waste cast in concrete, in both 1 BTF and 2 BTF, a concrete slab with a thickness of 50 cm will be placed.

Length:	160 m
Width:	15 m
Height of walls:	6.5 m
Height of tunnel arch:	3 m
Total height:	9.5 m
Total volume:	19,700 m^3

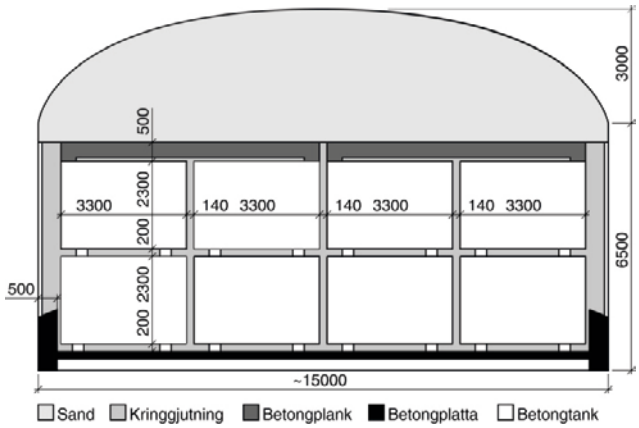

Figure 1-3. *Repository rooms 1 BTF and 2 BTF.*

Length:	160 m
Width:	15 m
Height of walls:	9 m
Height of tunnel arch:	3.5 m
Total height:	12.5 m
Total volume:	27,600 m^3

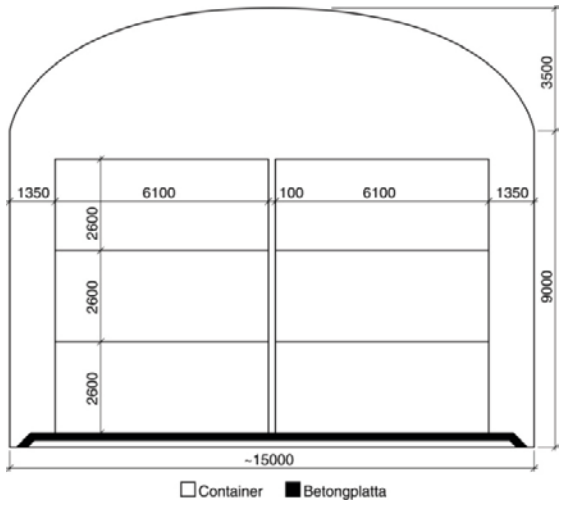

Figure 1-4. *Repository room BLA.*

The space between the waste and the rock wall will be filled with concrete, except for the 50 mm closest to the rock wall where a sheet of rock wool will be placed for drainage. The space above the concrete slab, as well the loading and transshipment zone, will be filled with sand.

1.2.3 Repository room BLA

The geometry of repository room BLA can be seen in Figure 1-4.

Type of waste and backfill

The waste is low–level solid waste such as trash and scrap stored in containers and stacked on each other up to a height of approximately 8 m. No re-filling is planned in the repository room where the waste is stored or in the loading and transshipment zone.

1.2.4 Repository room BMA

The geometry of repository room BMA can be seen in Figure 1-5.

Length:	160 m
Width:	19.6 m
Height of walls:	11.5 m
Height of arch:	5 m
Total height:	16.5 m
Total volume:	47,650 m^3

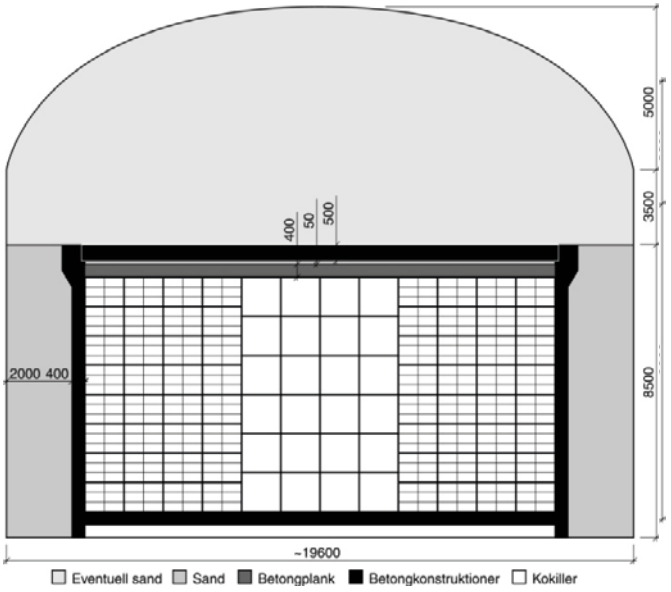

Figure 1-5. *Repository room BMA.*

Type of waste and backfill

The waste is intermediate-level solidified waste stored in 13 rooms with walls of concrete having a thickness of 40 cm. On top of the rooms, a concrete slab with a thickness of 40 cm is placed. After that, a layer of concrete with a thickness of 5 cm is cast. Finally, when the room is sealed, a cap of reinforced concrete is cast on the top of the structure. The total height of the concrete structure will be 8.5 m. The void spaces in the rooms can be filled with concrete of low viscosity.

Along the sides of the rooms, between waste and rock wall, sand is placed. Sand is also placed in the loading and transshipment zone. The void space above the concrete cap can be filled with sand or remained unfilled. In the analysis presented in this report the space above the concrete cap is not filled with sand.

1.3 Experience from the operation of SFR

The experience from the excavations of the SFR rock caverns and silo, shows clearly that the quality of the rock mass within the construction area is such that it lends itself to excavation of large rock caverns with a minimum of rock support (Calsson and Christiansson 2007). After taken into operation, the underground facility of the SFR has been subjected to recurrent inspections with regard to rock quality and rock support. The result from various inspections, testing and measurements carried out during the operation since 1988 do not indicate any significant deterioration or failure of installed rock support. The host rock mass after excavation has performed as foreseen, and no stability problems or unexpected deformation have been observed, nor has any problem related to groundwater inflow been identified. For more details, see Carlsson and Christiansson (2007).

2 Input to the calculations

2.1 Fracture network

The basic data that has been used for the derivation of the fracture orientations has been the mapping at site of the cavern walls at the time of construction (Christiansson and Bolvede 1987). An example of the mapping of the cavern walls can be seen in Figure 2-1.

When analyzing geologic mapping it is important to consider that graphical representations are always generalized due to the scale of the presentation. Dominant or regular structures are always represented graphically, whereas less frequently occurring structures are shown only to the extent to which they are determined to affect stability. Similarly generalizations can be made where a series of short fractures, with the same orientations and in close succession to each other, may be represented graphically as one long fracture.

Based on the mapping of the cavern roof and walls, three joint sets have been identified. These are shown in Table 2-1. The orientations of the joints are given with respect to the longitudinal axis of the rock caverns. The orientation of the caverns is N30E.

Based on the data in Table 2-1 and the fracture mapping of the caverns, a simple DFN (Discrete Fracture Network)-model consisting of three fracture sets has been derived. In order to verify the model, the joint traces on the walls of the caverns generated with the DFN-model have been compared with the traces from the mapping of the caverns. In the DFN-model, orientation of the fracture sets together with intensity and size of the fractures have been adjusted in order to obtain a visual agreement between generated and mapped fracture traces.

In Figure 2-3 the fracture pole orientations for a generated fracture network are presented.

Table 2-1. Fracture sets. Data given with max-min values.

Strike of fractures with respect to longitudinal axis of caverns [°]	Dip [°]	Average distance between fractures
13 ± 20	90 ± 5	2 m
97 ± 27	90 ± 14	2 m
0 ± 180	0 ± 17	3 m

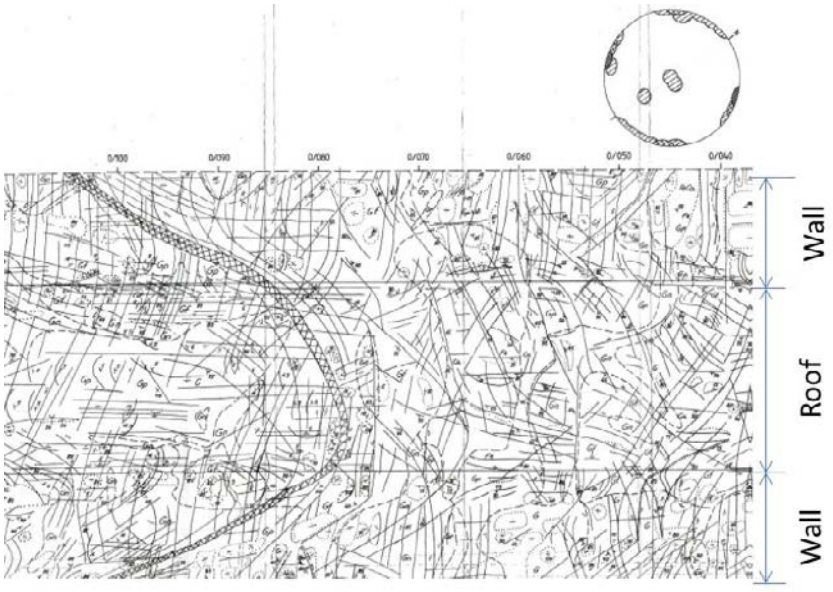

Figure 2-1. *Example of fracture mapping of the roof and walls at the BMA cavern.*

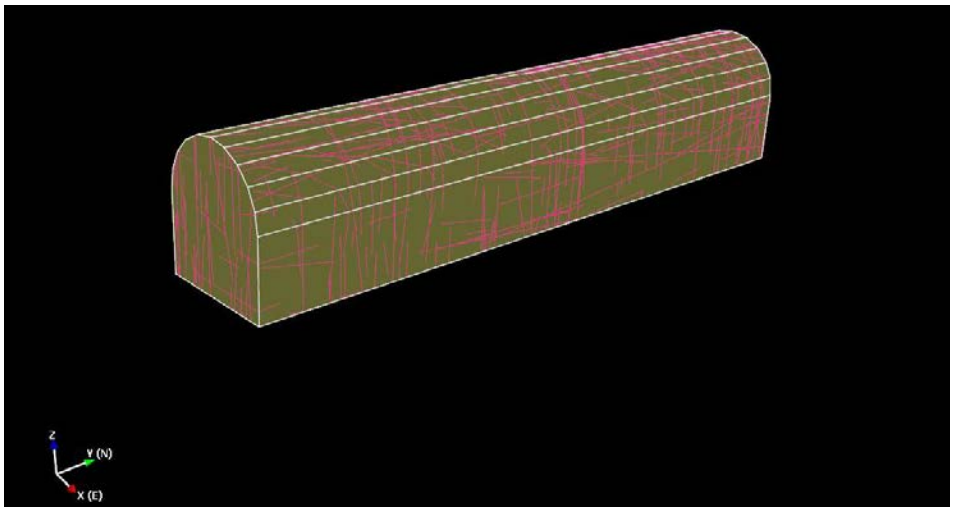

Figure 2-2. *Fracture traces on the cavern wall generated from the DFN model.*

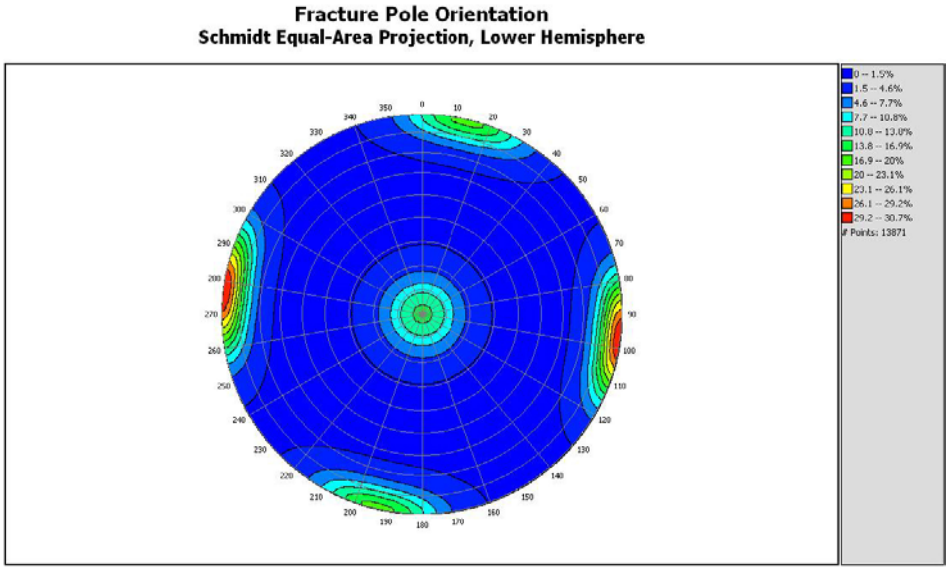

Figure 2-3. *Fracture pole orientations from a generated fracture network.*

2.2 Fracture zones

According to the fracture mappings of room BMA, there exist two distinct zones with fractured rock with a strike that is almost perpendicular to the caverns. Dip and dip direction of the first zone is 27 and 161 degrees respectively, while the dip and dip direction for the second zone is 70 and 25 degrees. The zones have a thickness of approximately 1.0 m. Based on the information from the mapping, two zones with a thickness of 1.0 m have been adapted to this information and extrapolated to the rock surface, see Figure 2-4.

2.3 Numerical model

The BMA room is widest and has a height of 16.5 meters. In room BLA and BMA no top filling is planned. The waste in BLA can be compressed. Therefore no waste is included in room BLA. In order to decrease the calculation time only room BMA and BLA are included in the numerical model. Symmetry is assumed between the caverns 2BTF and BLA. In the numerical model, the rock mass has been modeled as a block with two persistent zones, see Figure 2-5. The dimensions of the block are 240 × 140 × 100 m.

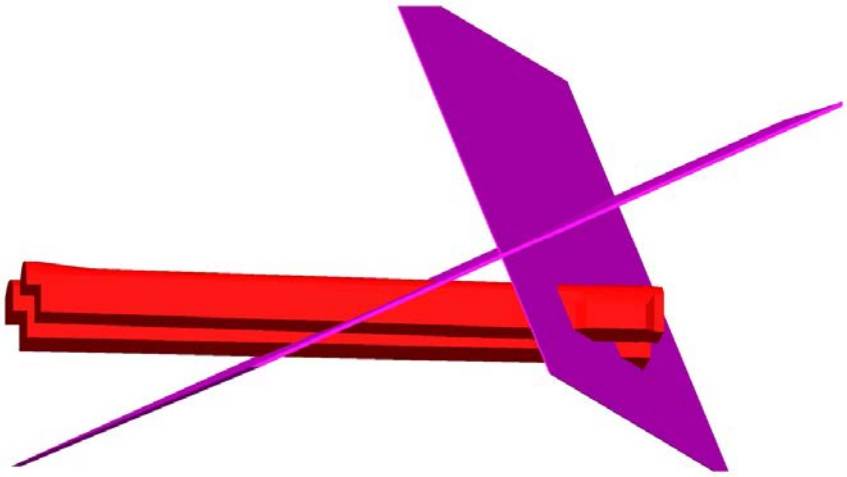

Figure 2-4. *Illustration of zones with fractured rock.*

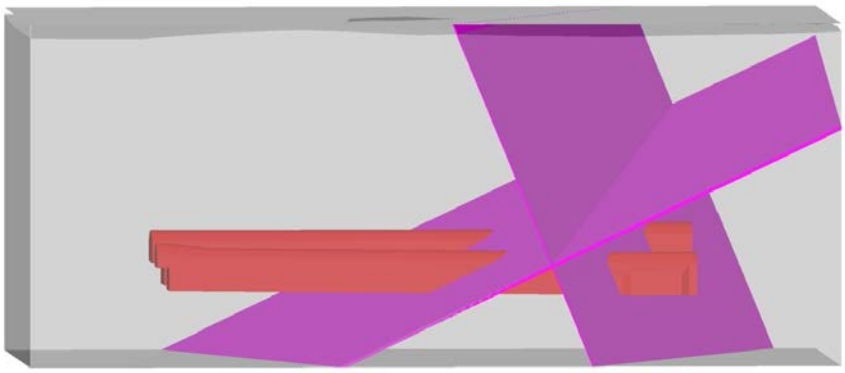

Figure 2-5. *Dimensions of the model, 240 × 140 × 100 m.*

2.4 Material properties

2.4.1 Rock between fractures

Mechanical properties for the intact rock between represented fractures in the models have been assumed based on the values in Glamheden et al. (2007a). The values are presented in Table 2-2. The intact rock is considered isotropic.

2.4.2 Fracture zones

In Glamheden et al. (2007a) a back analysis of the mechanical properties of the weakness zone "Singö-zone" has been performed. Based on the properties for this zone derived from the analysis, properties according to Table 2-3 have been assumed for the existing weakness zones in this analysis.

Table 2-2. Properties for rock mass between fractures.

Modulus of deformation [GPa]	Poisson´s ratio [–]	Friction angle [°]	Cohesion [MPa]	Tensile strength [MPa]	Dilation angle [°]
60	0.23	40	23.3	–6.8	15

Table 2-3. Properties for the weakness zones with fractured rock.

Modulus of deformation [GPa]	Poisson´s ratio [–]	Friction angle [°]	Cohesion [MPa]	Tensile strength [MPa]	Dilation angle [°]
16	0.43	51	2.0	–0.1	15

2.4.3 Fractures

In the numerical analysis, calculations of stresses and deformations for the caverns under realistic conditions as well as calculations with successive reduction of the fracture properties are performed. It is therefore of interest to both sets of analyses to assign realistic values to the mechanical properties of the fractures and to discuss the lowest values of the friction angles that are possible.

An empirical peak shear strength criterion has been developed by Barton and Choubey (1977), which is expressed as follows:

$$\tau_p = \sigma_n \tan\left[JRC \log_{10}\left(\frac{JCS}{\sigma_n}\right) + \phi_b\right] \quad (2\text{-}1)$$

Where JRC is the Joint Roughness Coefficient that quantifies roughness, JCS is the Joint Wall Compression Strength of the rock surface, and ϕ_b is the basic friction angle on dry saw-cut surfaces. The residual friction angle ϕ_r is used instead of ϕ_b if the strength of wet surfaces is considered.

The JRC and JCS parameters are dependent on fracture length. Therefore, the measured values are normalized and extrapolated to values that relate to a standard fracture length of 100 mm, and referred to as JRC_{100} and JCS_{100} values.

For a given level of stress, the relation in Equation 2-1 can be linearly approximated to determine the peak friction angle and cohesion of the Mohr-Coulomb Strength Criterion as:

$$\tau_p = c_p + \sigma_n \tan \emptyset_p \quad (2\text{-}2)$$

where, c_p and ϕ_p are peak cohesion and peak friction angle. Similarly, the residual cohesion, c_r and residual friction angle ϕ_r can be fitted by the Mohr-Coulomb residual envelope.

During the site characterization of the Forsmark site a number of tilt tests were performed in order to evaluate the strength of fractures (Glamheden et al. 2007b). Variation of the evaluated parameters with depth, that is basic friction angle, residual friction angle, JRC_{100} and JCS_{100} are shown in Figure 2-6 and Figure 2-7. The basic and residual friction angles display a small increase with depth in Figure 2-6. JRC_{100} and JCS_{100} display no variation with depth in Figure 2-7. Most of the testing is from a greater depth than the SFR. The depth of SFR is indicated in the figures. Results from all tilt tests are presented in Table 2-4.

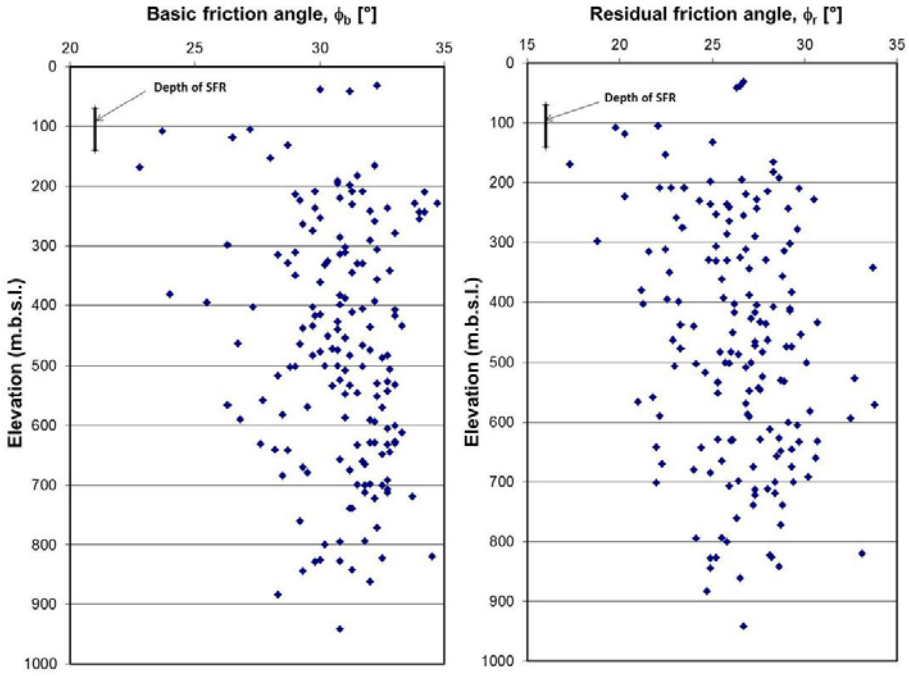

Figure 2-6. *Basic friction angle and residual friction angle versus depth.*

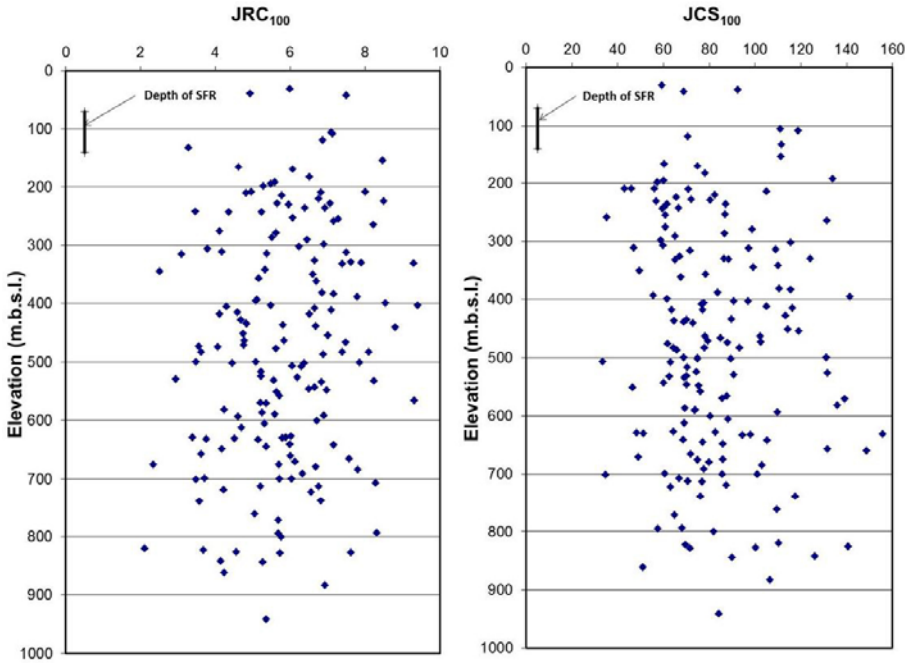

Figure 2-7. *JRC_{100} and JCS_{100} (MPa) versus depth.*

Table 2-4. Test results from 163 tilt tests.

	Minimum	Mean	Median	Maximum	Standard deviation
Basic friction angle (°)	22.8	30.8	31.2	34.7	2.0
JRC_{100}	2.1	5.8	5.8	9.4	1.5
JCS_{100} MPa	33	83	77	156	25
Residual friction angle (°)	17.3	26.4	26.7	33.8	2.9

The linear Mohr-Coulomb envelope has been fitted to the curved Barton-Bandis envelope in the stress range from 0–20 MPa (Glamheden et al. 2007b). The Mohr-Coulomb model parameters are presented in Table 2-5.

In a study of passing the Singö deformation zone with the SFR tunnels (Glamheden et al. 2007a), the properties of rock fractures in the vicinity of Singö zone have been determined as summarized in Table 2-6. Those properties have been used as initial fracture properties for the models in this study.

Table 2-5. Calculated results from 163 tilt tests.

Parameter	Minimum	Mean	Median	Maximum	Std.dev
ϕ_p, °	25.8	33.8	33.9	37.7	1.9
c_p, MPa	0.2	0.5	0.5	0.8	0.1
ϕ_r, °	20.3	29.4	29.6	37.9	3.0
c_r, MPa	0.2	0.4	0.4	0.7	0.1

Table 2-6. Properties of rock fractures used as initial properties in the models.

Friction angle, ϕ_r [°]	Cohesion, c_r [MPa]	Normal stiffness [GPa/m]	Shear stiffness [GPa/m]
25.0	0.05	80.0	2.0

A fracture shear dilation angel of zero degrees has been used in all the models. This assumption is on the conservative side. No water pore pressure has been considered in the fractures. This is not on the conservative side, but the water pressure should be corresponding to about 60 m ground water level (ca 0.6 MPa), which means a moderate influence on the effective stress. The influence will depend on the orientation of the fracture planes (note that these calculations do not concern the glacial time period when water pressures can be higher).

When a rock fracture is subjected to weathering the Joint Wall Compression Strength, JCS of the rock surface is decreased. When the ratio of JCS/σ_n approaches 1.0 the joint shear strength becomes:

$$\tau_r = \sigma_n \tan \emptyset_r \qquad (2\text{-}3)$$

Therefore the residual friction angle, ϕ_r, of a fracture represents the minimum shear strength of the fracture.

The residual friction angle of a fracture depends on the fracture filling material. Results of tilt tests carried out on fractures without filling show a lowest (or 'minimum') residual friction angle of about 17° for the Forsmark area, see Figure 2-6.

The engineering geology follow-up from the time of construction at 1987 showed that the rock mass at the site is dominated by granite and granite-gneiss with dykes of greenstone and pegmatite. The granite and granite-gneiss mainly is composed by quartz, feldspar and mica. According to Horn and Deere (1962) the friction coefficient under saturated conditions is 0.45 (24°) for quartz, 0.77 for feldspar (38°) and 0.13 (8°) for biotite mica. In general, the infilling material in the joints due to weathering of the granite and gneiss-granite could therefore be expected to have a friction angle somewhere around the average value from these minerals, which is 23°. Locally, where the concentrations of sheet minerals are higher, this value could be lower.

Barton (2002) shows residual friction angles between 8–16° for fractures with 1–2 mm filling consisting of chlorite, talc, gypsum and graphite. A realistic residual friction angle for weathered fractures in the Forsmark area would be 15–17°. An absolute lowest residual friction angle for weathered fractures in the Forsmark area would be approximately 8°.

2.4.4 Infilling material in repository room BMA

Assumed properties of the filling material in the repository room BMA are presented in Table 2-7 and Table 2-8 for concrete and sand respectively. The moduli are the long term modulus.

2.5 In situ stresses

Based on the interpretation of the in situ stress measurements presented in SKB (2002), initial in situ stresses according to Table 2-9 have been assumed. The major principal stress is oriented perpendicular to the caverns.

Table 2-7. Properties for the concrete.

Modulus of deformation [GPa]	Poisson´s ratio [–]	Friction angle [°]	Cohesion [MPa]	Tensile strength [MPa]	Dilation angle [°]
17	0.15	38	8.17	1.05	10

Table 2-8. Properties for the sand.

Modulus of deformation [MPa]	Poisson´s ratio [–]	Friction angle [°]	Dilation angle [°]
6	0.3	32	15

Table 2-9. In situ stresses.

σ_H, MPa	σ_h, MPa	σ_v, MPa
4.8 + 0.095 · z	1.4 + 0.028 · z	0.027 · z

3 Methodology

3.1 Numerical analyses with 3DEC

In order to model the successive decomposition of the rock mass due to long term degradation, numerical calculations with the program 3DEC have been performed. In the calculation model the northern part of the repository rooms 1 BMA and 1BLA have been included, see Figure 2-5**.** In 3DEC, the following modeling sequence has been used:

1. Solve model with initial properties in elastic mode.
2. Change to Mohr-Coulomb intact rock properties and Coulomb slip fracture properties and solve until equilibrium.
3. Solve model after excavation of caverns.
4. Solve model after filling with sand and concrete in room 1 BMA.
5. Solve model after fracture properties have been reduced in a zone around the tunnel.
6. The previous step is repeated until blocks begin falling (runs with deformable blocks) or the tunnels are full of blocks (runs with rigid blocks).

3.2 Analyzed models

Two main types of models have been analyzed in 3DEC; models with deformable blocks and models with rigid blocks.

With the deformable models, eight cases with eight DFN realizations have been analyzed. A different fracture random generator is used for each case. All fracture planes of the different fracture sets have been modeled as perfectly planar, infinite structures, which is considered to be conservative. The simulation is stopped once significant displacements are observed. Based on this, the critical friction angle (when blocks start to fall) for the fractures can be obtained. Only eight realizations were simulated because these simulations are very computationally intensive, each one took around three months to finalize. However, with each model encompassing 100 meters of length in each cavern, the authors believe that the critical block configuration will be represented with good certainty in each one of the simulation cases. The similar results obtained in each of the cases supports this idea.

With the rigid models, two cases have been analyzed. In the first case vertical and horizontal fracture sets are used without any standard deviation in strike and dip. In the second case, the vertical and horizontal fractures are generated with a specific standard deviation (the same as in the case of deformable blocks, see Table 2-1, but only one DFN realization, the one called Ref. case in Figure 4-5). The reason for running rigid models is that they run significantly faster and they represent the worst case scenario with respect to deformable block models. They were used to assess the capability of the caverns to be self-sustaining due to the bulking effect if, in case of total collapse, rock blocks fill the caverns. These simulations were stopped once the tunnels were filled with blocks and surface displacements had stabilized.

In all models, the two fractured zones described in Chapter 2.2 have been included. The reason for this is that they may influence the mechanical behavior of the rock mass adjacent to the tunnels.

The numerical model with deformable blocks has been divided into two zones, one outer zone and one inner zone. In the inner zone, the fractures are generated with a higher density (spacing 2–3 m, see Table 2-1). This zone corresponds to the center section of the tunnels between the deformation zones. For the outer zones, a lower fracture set density is used with a spacing of 6 m. The dimensions of the numerical model can be seen in Figure 3-1.

In the numerical model with rigid blocks the same density (spacing) is used up to the surface and the model extends up to the actual rock surface, see Figure 4-3.

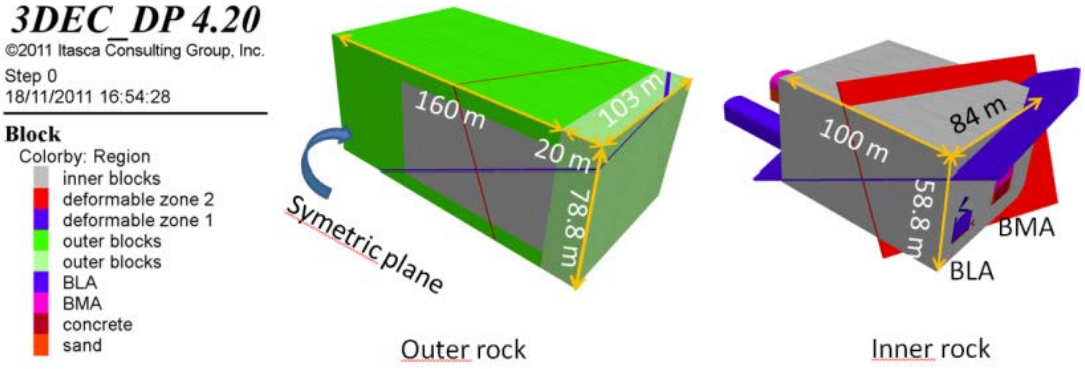

Figure 3-1. *Dimensions of the numerical models with deformable blocks.*

3.3 Reduction of material properties for the rock mass

The performed analysis simulates the results when existing rock support has been completely degraded. After that, the rock mass will be slowly degraded through different weathering processes. These processes mainly occur in existing fractures, which means that the properties of the intact rock will not be changed appreciably in these processes. The properties of the intact rock will therefore not be reduced in 3DEC.

However, the properties of the fractures will be reduced in a series of steps, n. The properties will be reduced in a specific volume that is defined by the radius $r_{red,n}$. This radius increases with a specific distance δr for each step according to the following equation:

$$r_{red,n} = r_i + n \cdot \delta r \tag{3-1}$$

Where r_i is the radius of the tunnel in meter. δr is set to 0.5 m. The shear strength of the fractures is described according to:

$$\tau_n = c \cdot r_{c,n} + \sigma_n \cdot (tan\emptyset) \cdot r_{\emptyset,n} \tag{3-2}$$

Where t_n is the shear resistance for reduction step n, c is the cohesion of the fracture, s_n is the normal stress and f is the friction angle of the fracture. $r_{c,n}$ and $r_{f,n}$ is reduction factors for cohesion and friction coefficient respectively described as:

$$r_{c,n} = n - n \tag{3-3}$$

$$r_{\emptyset,n} = a^{n-1} \tag{3-4}$$

Where a is a reduction factor assumed to be 0.9. With the equation above, the cohesion will be reduced to zero in the first step while the coefficient of friction will be the same. In the subsequent steps, the cohesion will be zero and the coefficient of friction will successively be reduced for each step. An example of how the coefficient of friction is reduced is presented in Figure 3-2.

The normal and shear stiffness, K_N and K_S will be reduced with the same methodology as the coefficient of friction according to:

$$K_{N,n} = K_N \cdot r_{\emptyset,n} \tag{3-5}$$

$$K_{S,n} = K_S \cdot r_{\emptyset,n} \tag{3-6}$$

The equations above do not consider that the degradation of the rock mass will be more pronounced closest to the tunnel wall and thereafter be less pronounced deeper into the rock mass. In order to account for this effect, the rock mass is divided into different zones where each zone is defined as the difference between two different reduction radius.

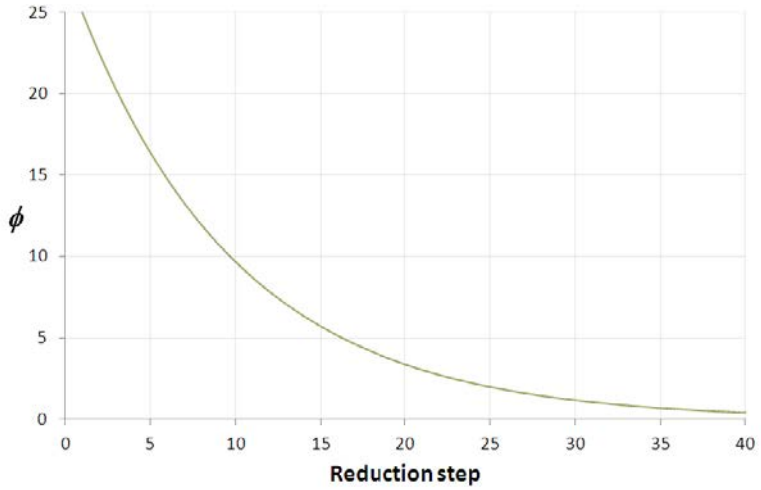

Figure 3-2. *Reduction of the friction angle as a function of reduction step.*

This means that the reduction of the mechanical parameters of the fractures has been performed in such a way that the outer zone will only have a reduced cohesion while the coefficient of friction will be un-reduced. On the other hand, in the zone closest to the tunnel wall, both the cohesion and the coefficient of friction will be reduced, provided that several reduction steps have been performed. In other words, the major reduction of the properties will be in the zone closest to the tunnel wall while the minor reduction will take place in the zone furthest into the tunnel. The methodology is described in Figure 3-3. In Figure 3-4 are shown the fracture property reduction zones for different reduction steps for one of the analyzed case. It should be noted that with the following methodology, the degradation could only be considered to be correlated to time and distance. No specific consideration has been taken to other parameters that might affect the intensity and extent of the degradation, e.g. the extents of zones of fractured rock, stress distribution or displacements in the rock mass. However, the used methodology is considered to be acceptable with respect to the objectives of the report.

In addition, it could be discussed if a model with uniform shear strength along the tunnel axis could represent real conditions with respect to the anticipated spatial variation of the shear strength of the fractures. In general, failures will be initiated at areas with low local values. Due to this, the friction angles reached in the calculations when failure is initiated could be considered to constitute a measure of these local areas with lower friction angles. With this approach of looking at the results, the effect from spatial variation could indirectly be considered to be accounted for.

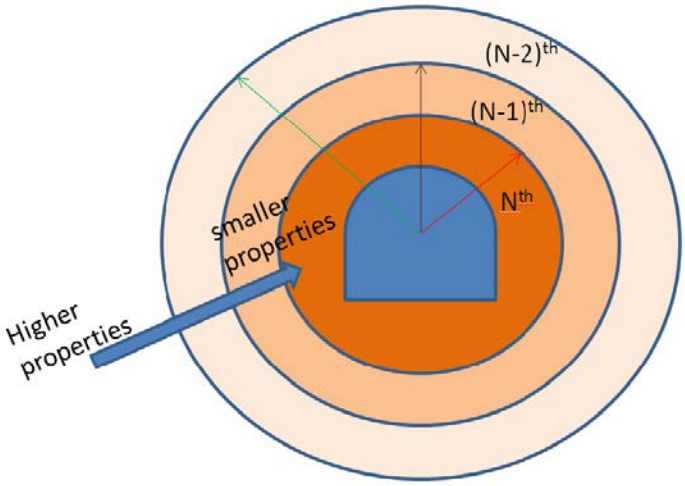

Figure 3-3. *Division into zones within the reduced part of the rock mass.*

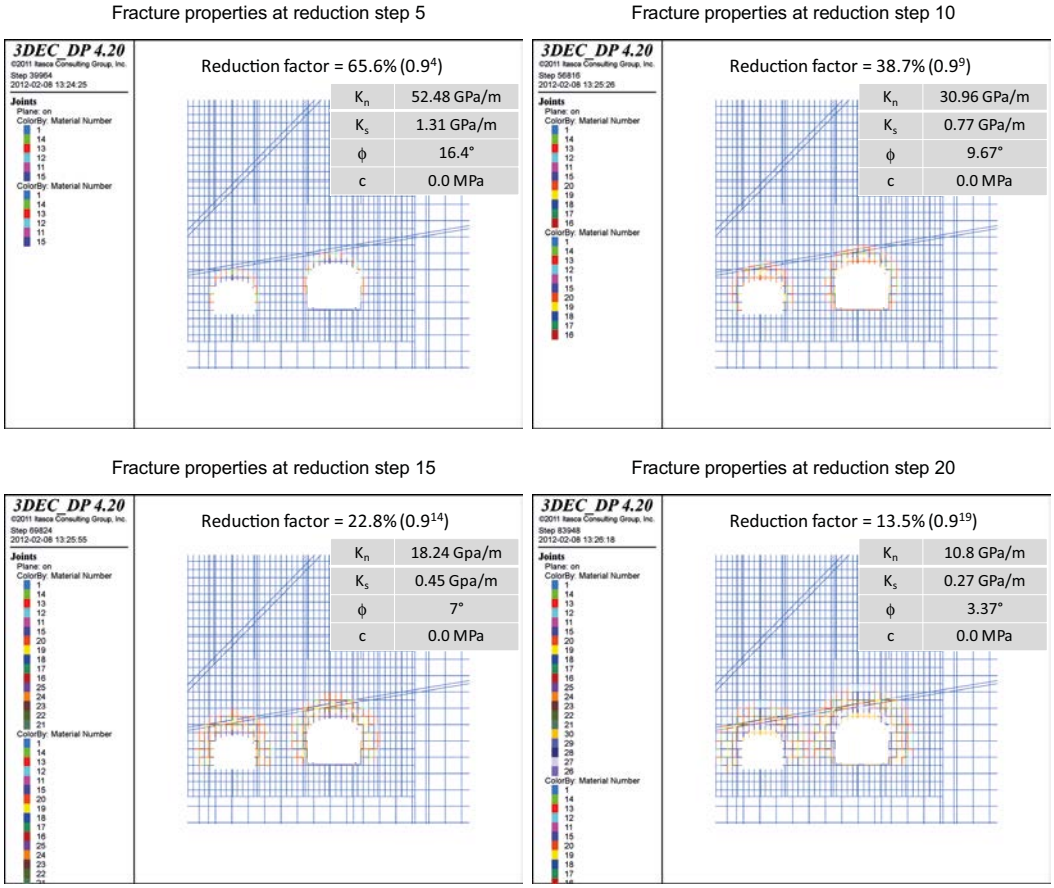

Figure 3-4. *Schematic figure showing the evolution of the fracture property reduction zone around both caverns as modeled in the case with no standard deviation in fracture orientation. The properties in the grey box are the ones assigned to the reduced volume closest to the cavern boundaries (the most reduced zone).*

4 Analysis and results

To address the different open questions according to the objectives of the project a number of models have been run. The following sections present in a detailed manner the model setup for the different cases analyzed and the results obtained.

4.1 Model setup

Two main types of models have been used in the study; deformable block models and rigid block models. The difference between them is that in the rigid block models the blocks in between fractures are rigid and therefore the stress is only calculated in the fracture planes not inside the blocks. On the other hand, in the deformable block models, the blocks between fracture plains are discretized in small tetrahedral zones and therefore stress can be calculated in the blocks as well. The deformable models have been run up to the point when noticeable displacements are generated at the boundary of the caverns and therefore blocks are beginning to fall. The rigid models are much faster to run than the deformable ones and they have been used to let the blocks fill up the caverns completely to study if the caverns, once completely filled with blocks, are self-supporting.

4.1.1 Model geometry

Deformable block model

The geometry dimensions for the deformable block model are presented in Figure 3-1, Figure 4-1 and Figure 4-2. In order to speed-up the simulations the upper boundary in the deformable block models is 20 m below the actual surface. This allows us to decrease the number of tetrahedral zones in the model to increase the speed of each calculation step. The in situ stress state is established taking this into account.

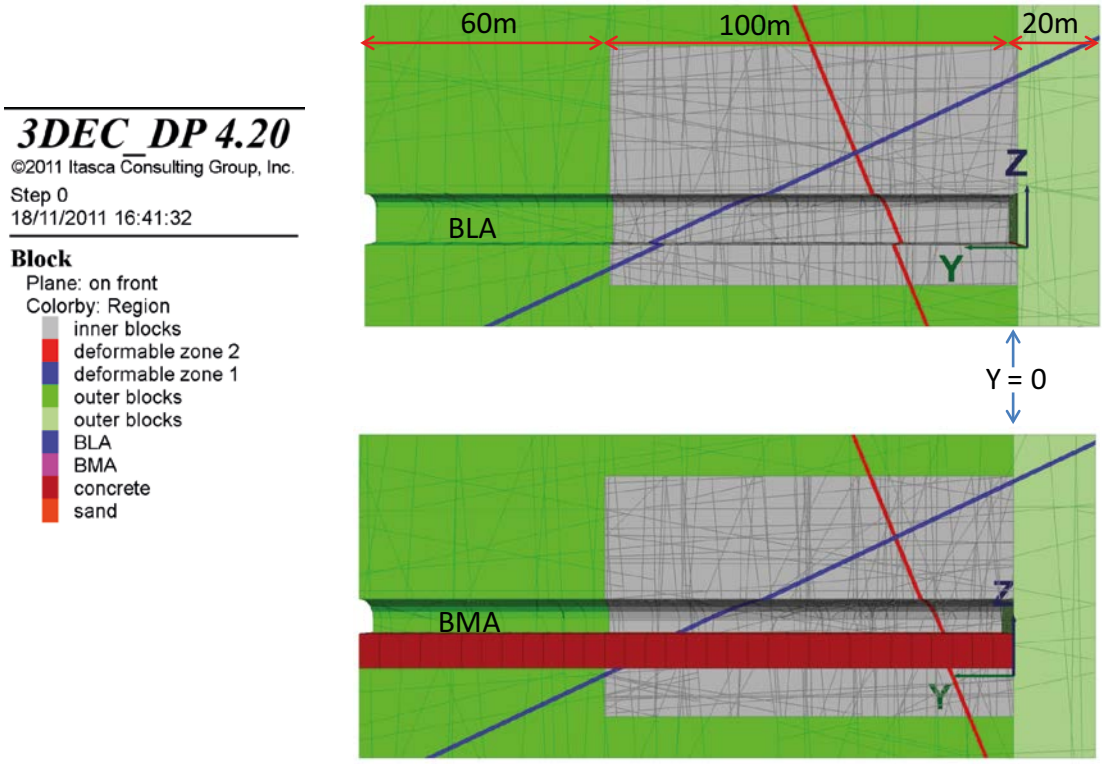

Figure 4-1. *Cross sections showing the dimension of the deformable block model. Notice the Y-coordinate origin and direction. Different cross-sections will refer to the Y-coordinate origin in this plot.*

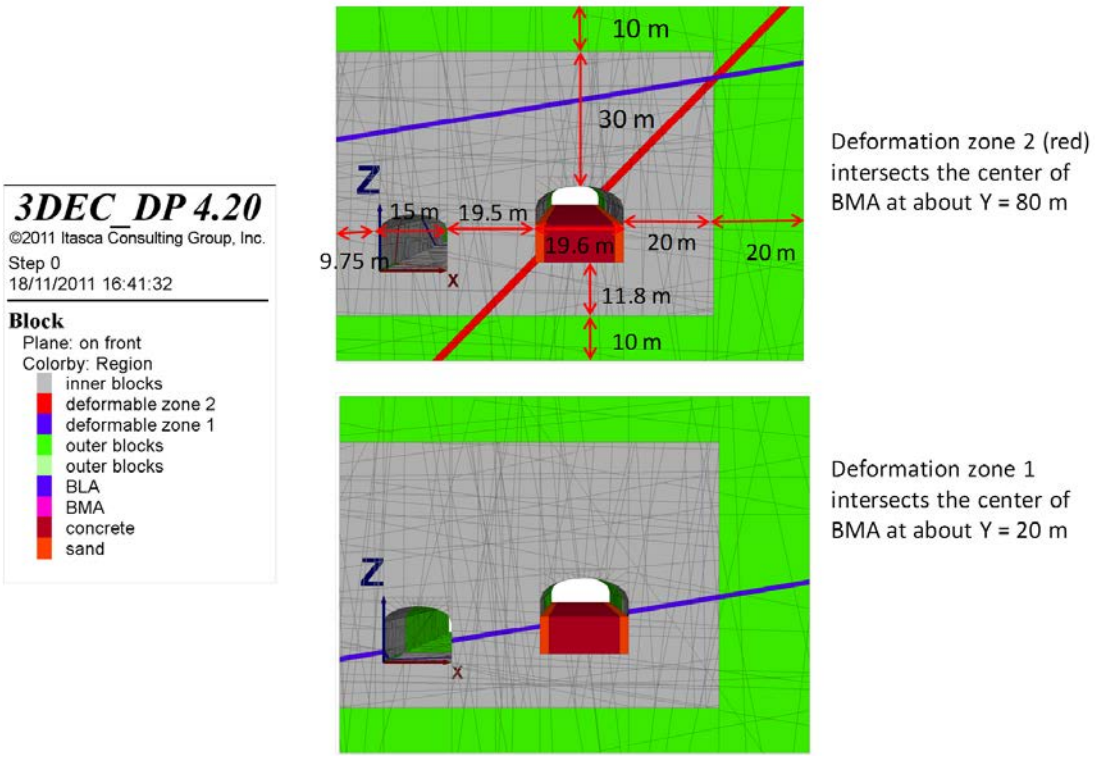

Figure 4-2. *Geometry and dimensions of numerical models with deformable blocks.*

Rigid block model

In the case of the rigid block model, the geometry is exactly the same as in the deformable block models but it extends up to the actual surface (see Figure 4-3) by adding the 20 m removed from the deformable block model. In this case the inner zone (clear and dark grey) extends up to the surface as well.

4.1.2 Fractures and deformation zones

The fracture planes of the different fracture sets have been modeled as perfectly planar, infinite structures (Figure 4-4). The fact that the fracture planes are infinite is considered to be conservative.

The two deformation (fractured rock) zones of 1 m thickness have been included in the model as a 1 m thickness layer of softer and weaker material than the surrounding rock.

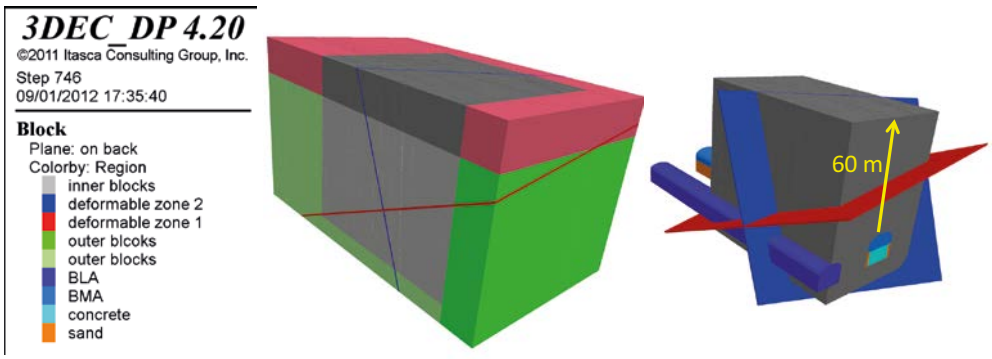

Figure 4-3. *Geometry of numerical model with rigid blocks.*

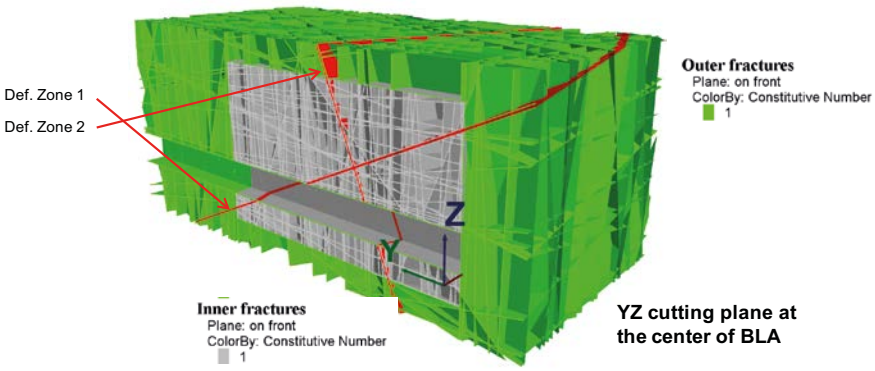

Figure 4-4. *YZ cutting plane at the center of BLA showing one of the realizations of the inner and outer fractures and the deformation zones.*

Eight models with eight DFN realizations were generated using 3DEC based on the fracture statistics in Table 2-1 using different random seed numbers. The stereo net plot of the fracture poles in each one of the realizations can be seen in Figure 4-5 to Figure 4-7.

One additional model with the same fracture statistics from Table 2-1 but without standard deviation in the orientation of the fracture planes has also been generated.

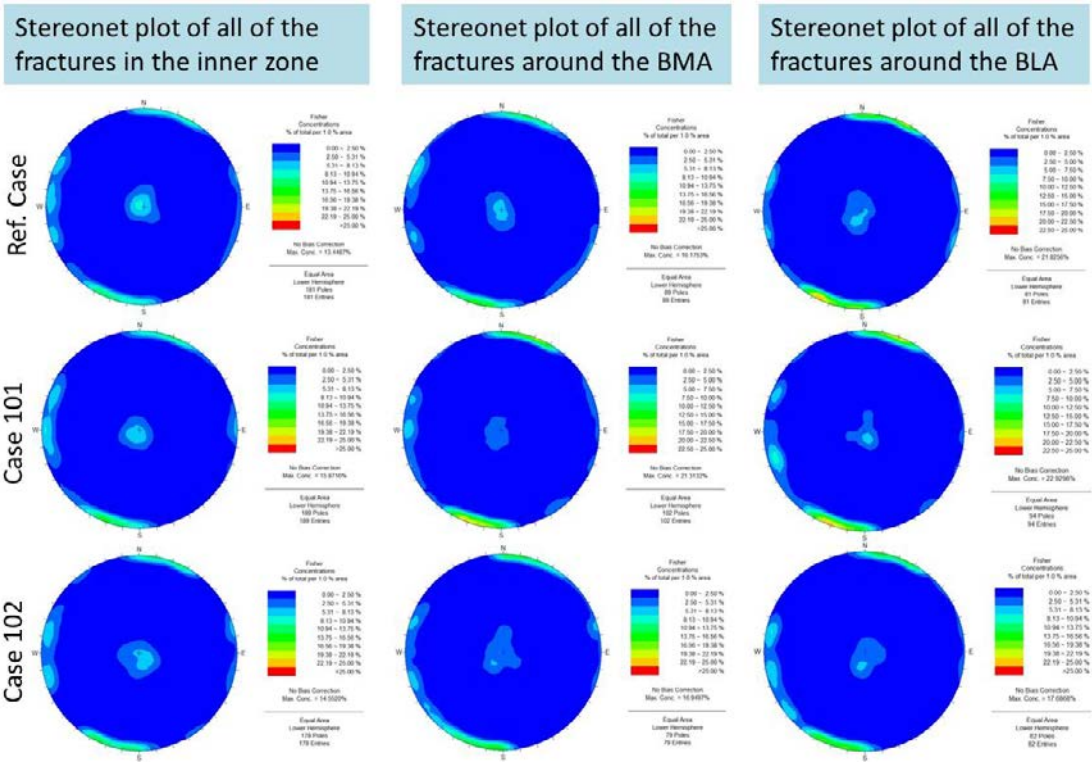

Figure 4-5. *Stereo net plot of the fracture poles in three different DFN realizations (reference case and random seed number 101, 102) based on the statistics in Table 2-1. To the left all the fractures in the inner zone, in the center all the fractures in a radius of 4 m from the boundary of BMA in the inner zone, to the right all the fractures in a radius of 4 m around the boundary of BLA in the inner zone.*

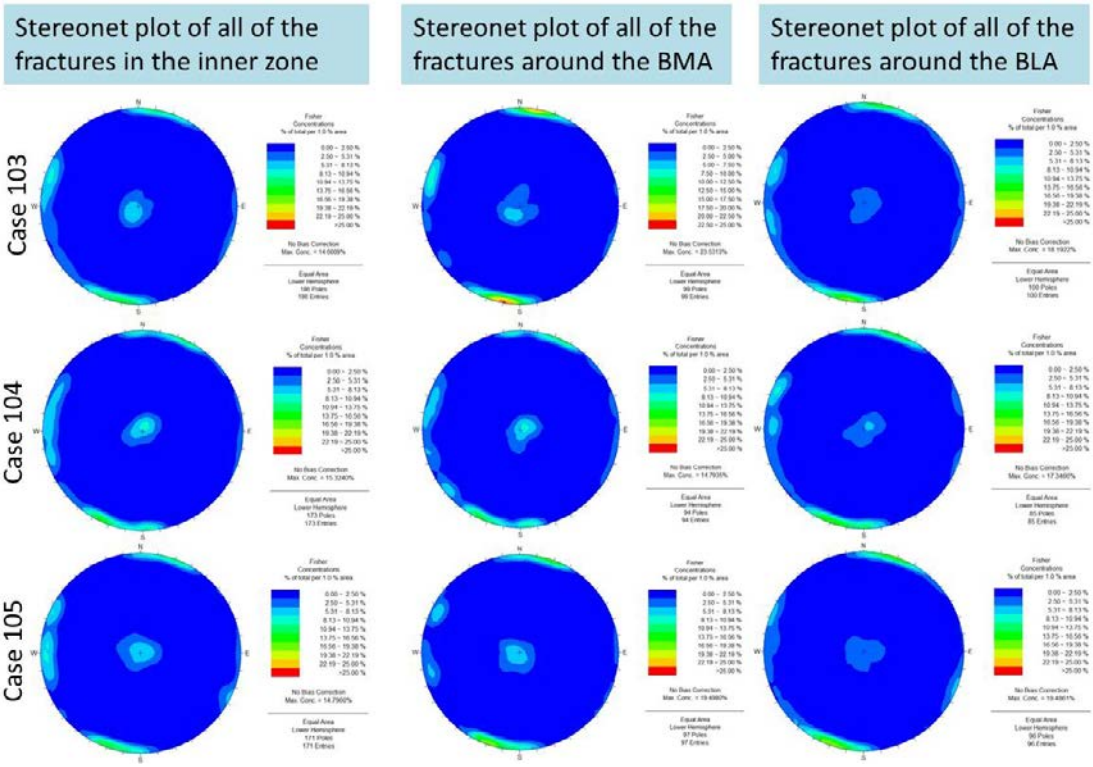

Figure 4-6. *Stereo net plot of the fracture poles in three different DFN realizations (random seed number 103, 104, 105) based on the statistics in Table 2-1. To the left all the fractures in the inner zone, in the center all the fractures in a radius of 4 m from the boundary of BMA in the inner zone, to the right all the fractures in a radius of 4 m around the boundary of BLA in the inner zone.*

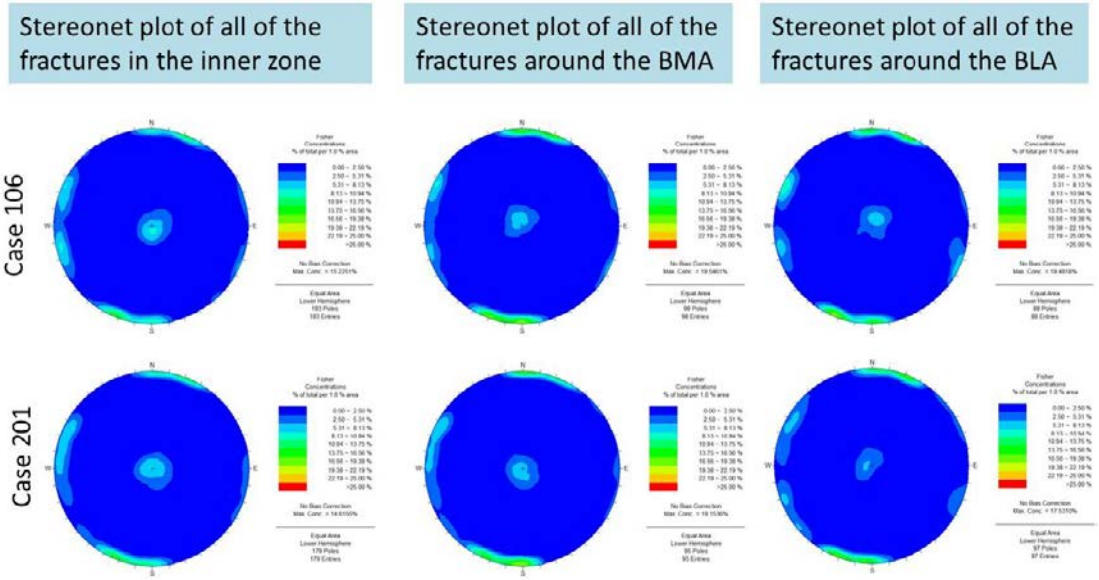

Figure 4-7. *Stereo net plot of the fracture poles in two different DFN realizations (random seed number106 and 201) based on the statistics in Table 2-1. To the left all the fractures in the inner zone, in the center all the fractures in a radius of 4 m from the boundary of BMA in the inner zone, to the right all the fractures in a radius of 4 m around the boundary of BLA in the inner zone.*

4.1.3 Boundary conditions

The boundary conditions used in the models are shown in Figure 4-8. They apply to both rigid and deformable block models.

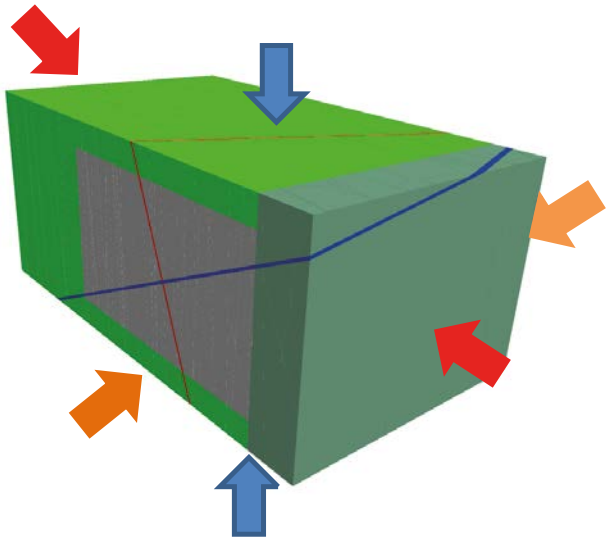

- Boundary stress is applied on the **top surface**
- Normal direction velocities are set to zero on the **left** and the **right** surfaces, the **front** and the **back** surfaces and on the **bottom surface**.

Figure 4-8. *Boundary conditions.*

4.1.4 Monitoring points

The criteria used in the models for evaluating tunnel stability were force-equilibrium and stable conditions in the rock mass. If force-equilibrium was reached without excessive rock-mass displacements, then stable conditions were achieved. Because 3DEC uses an explicit solution scheme, many calculation cycles are required before stable conditions may be achieved. In each calculation cycle, 3DEC determines an increment of displacement. This increment decreases when the solution approaches equilibrium. Hence, stable rock-mass conditions in the models are identified by displacements that reach constant acceptable values or velocities that become vanishingly small.

With this purpose, a number of displacement monitoring gauges were allocated at different locations in the caverns (Figure 4-9). These monitoring gauges were only used to follow the calculations to see if stable conditions are reached. The results from these gauges are not presented in the report.

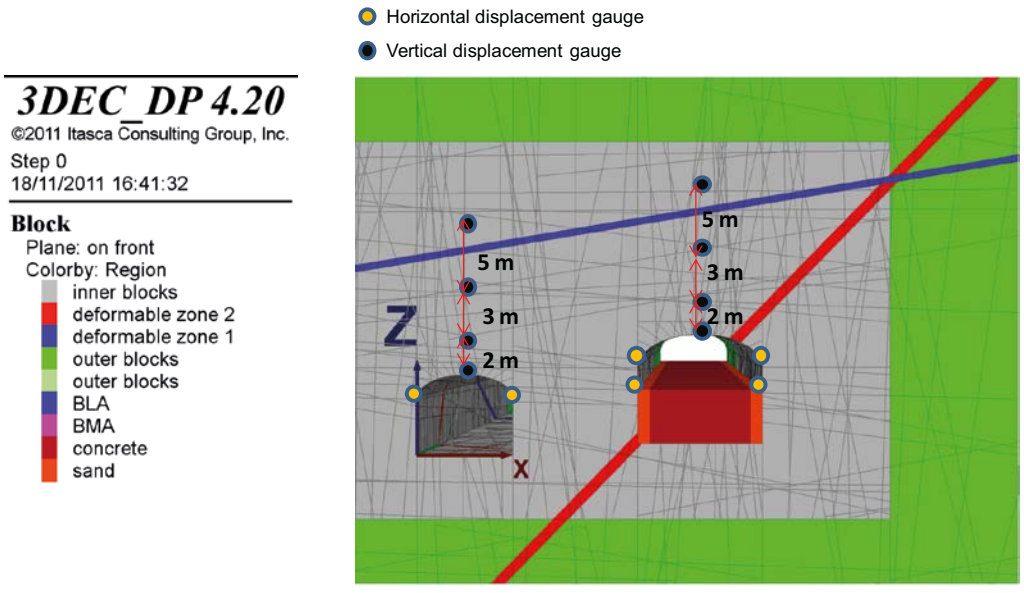

The displacement gauges are placed at different cross sections

- at y = 35.6, 48 and 60 m for BLA tunnel
- at y = 31.5, 45.5 and 59.5 m for BMA tunnel

Figure 4-9. *Schematic cross section showing the relative location of the displacement monitoring gauges in the model (not to scale). (See Y-coordinate origin orientation and direction in Figure 4-1.)*

4.1.5 In situ stress

Once the geometry of the models was completed the in situ stress was established. Figure 4-10 and Figure 4-12 present the maximum and minimum principal stress magnitude contours as modeled during the elastic equilibrium in the case with the DFN with random seed number 105. The influence of the displacements on fracture planes and deformation zones caused by the high maximum to minimum principal stress ratio is noticeable in the stress contours during equilibrium after the actual initial material properties (Mohr-Coulomb properties for the rock and Coulomb slip properties for the fractures) have been applied (Figure 4-11 and Figure 4-13).

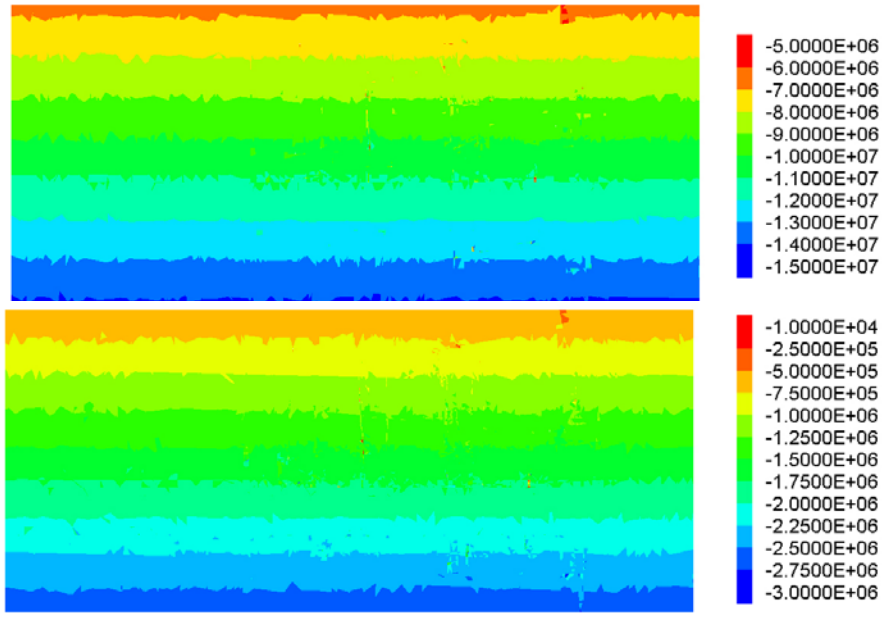

Figure 4-10. *Vertical cross sections parallel to the BLA tunnel through its middle showing maximum (above) and minimum (below) principal in situ stress magnitude contours (in Pa) in elastic mode (case 105).*

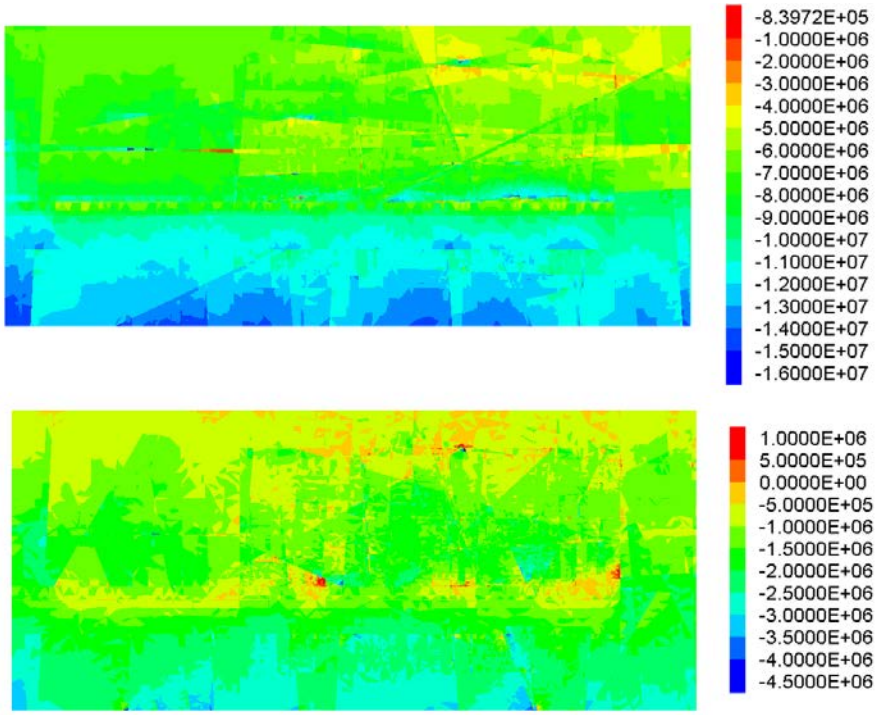

Figure 4-11. *Vertical cross sections parallel to the BLA tunnel through its middle showing maximum (above) and minimum (below) principal in situ stress magnitude contours (in Pa) once the actual Mohr Coulomb and Coulomb slip properties have been assigned to rock, deformation zones and fractures (case 105).*

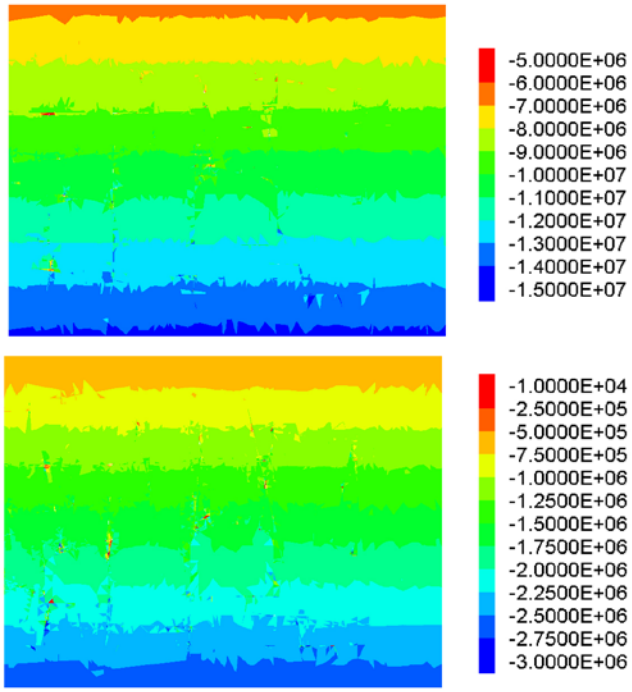

Figure 4-12. *Vertical cross section cutting perpendicular to the caverns at Y = 40 showing maximum (above) and minimum (below) principal in situ stress magnitude contours (in Pa) in elastic mode (Case 105).*

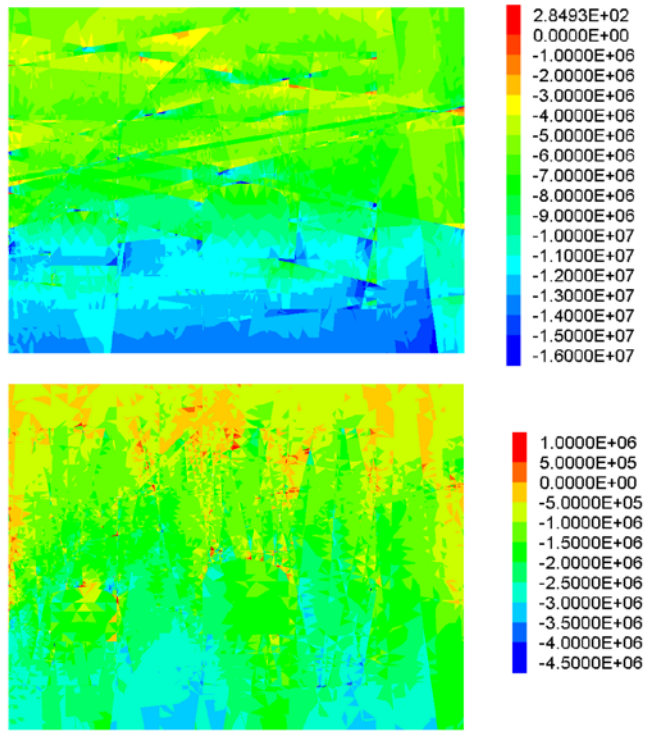

Figure 4-13. *Vertical cross section cutting perpendicular to the caverns at Y = 40 showing maximum (above) and minimum (below) principal in situ stress magnitude contours (in Pa) once the actual Mohr Coulomb and Coulomb slip properties have been assigned to rock, deformation zones and fractures (Case 105).*

4.2 Model results

This section presents the results of all the simulation cases considered in this study. All the cases were run following the modeling sequence described in Section 3.1 except a deformable block case with no standard deviation on the orientation of the fractures (Table 2-1). In that case the BMA cavern was excavated considering the sand and concrete are already present during the excavation stage. In this simulation the concrete and sand had the same properties as the rock material (Table 2-2). A "reference case" DFN run (Figure 4-5**)** was also run in a similar manner to be able to compare the results. These particular cases will only be discussed in Section 4.2.2 – Long Term Stability.

4.2.1 After excavation without reinforcement

The results discussed in this section come from the eight deformable block models with the DFN realizations presented in Section 4.1.2. It is important to note that no reinforcement has been modeled after excavation so this is a worst case scenario.

Vertical cross-section contour plots of the displacements and of maximum principal stress magnitude can be found in Figure 4-14 to Figure 4-29. These plots show a cross section perpendicular to both caverns at Y = 60 m and two cross sections parallel to the caverns axis cutting through the middle of both caverns.

For visualization purposes, the displacement value is limited to 0.01 m and to 0.15 m respectively for plots of excavation step and of the end of simulation (once the critical fracture friction angle has been reached). The maximum displacement remains small at the end of the excavation of the tunnels, 2~3 cm.

Figure 4-30 and Figure 4-31 present results of plasticity after excavation and at the critical fracture friction angle reduction step for the reference DFN case. The plots show that during the excavation step the only plastification of the rock occurs along the deformation zones, mainly in tension. The rest of the cases showed similar results.

To assess the stability of the excavation in the very worst case scenario an additional model (case 105, Figure 4-6 was run with initial fracture friction angle of 15° and no fracture cohesion. A scenario with fracture friction angle of 15° and no cohesion is judged to be the very worst but still realistic case scenario because according to the fracture data acquired at Forsmark the lowest residual friction angle is 15–17°, see Section 2.4.3. The DFN realization with random seed number 105 was chosen for this model. The results after excavation are shown in Figure 4-32 to Figure 4-37.

The maximum displacement in this case at the end of the excavation of the tunnels is between 2.5–5.5 cm depending on the tunnel section. Plasticity occurs only in the deformation zones and mainly in tension.

All the results presented in this section convey a system that is stable after excavation without reinforcement even in the worst possible case scenario when all the fractures in the model have a friction angle of 15° and no cohesion.

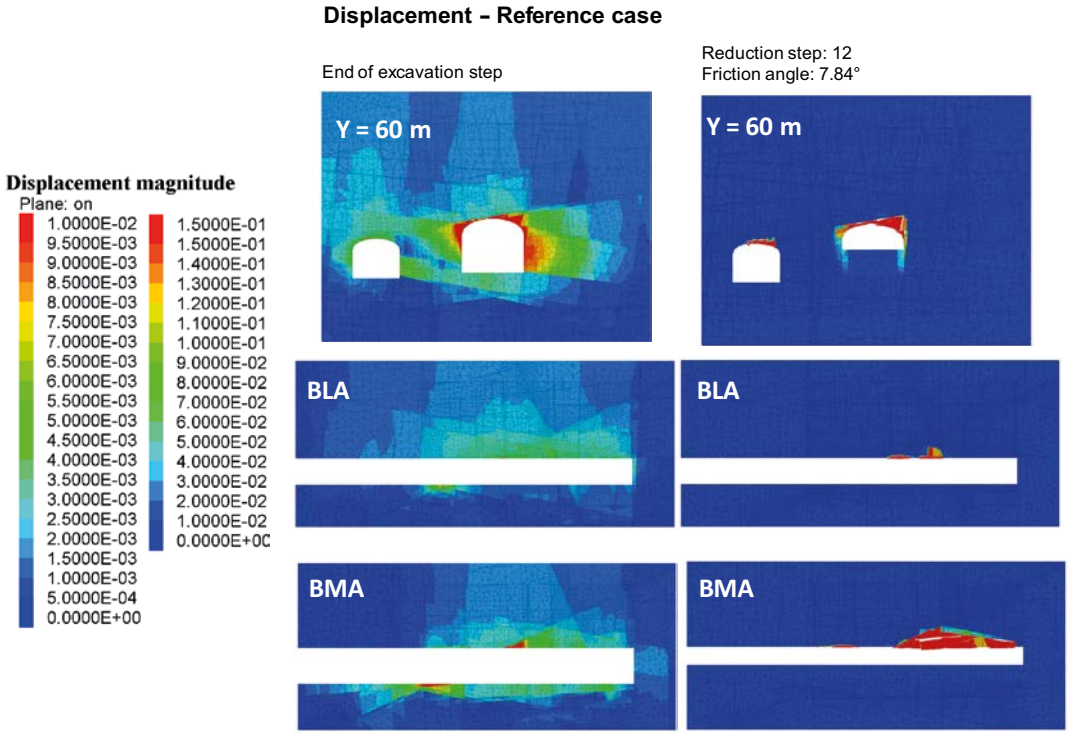

Figure 4-14. *Vertical cross-section contour plots of the displacements (in m) after excavation (left) and after the critical fracture friction angle has been reached (right) for the reference case. Cross section perpendicular to both caverns at Y = 60 m (upper) and two cross sections parallel to the caverns axis cutting through the middle of BLA cavern (middle) and BMA cavern (lower). The legend to the left is for the excavation stage and the one to the right is for the critical fracture friction angle plots.*

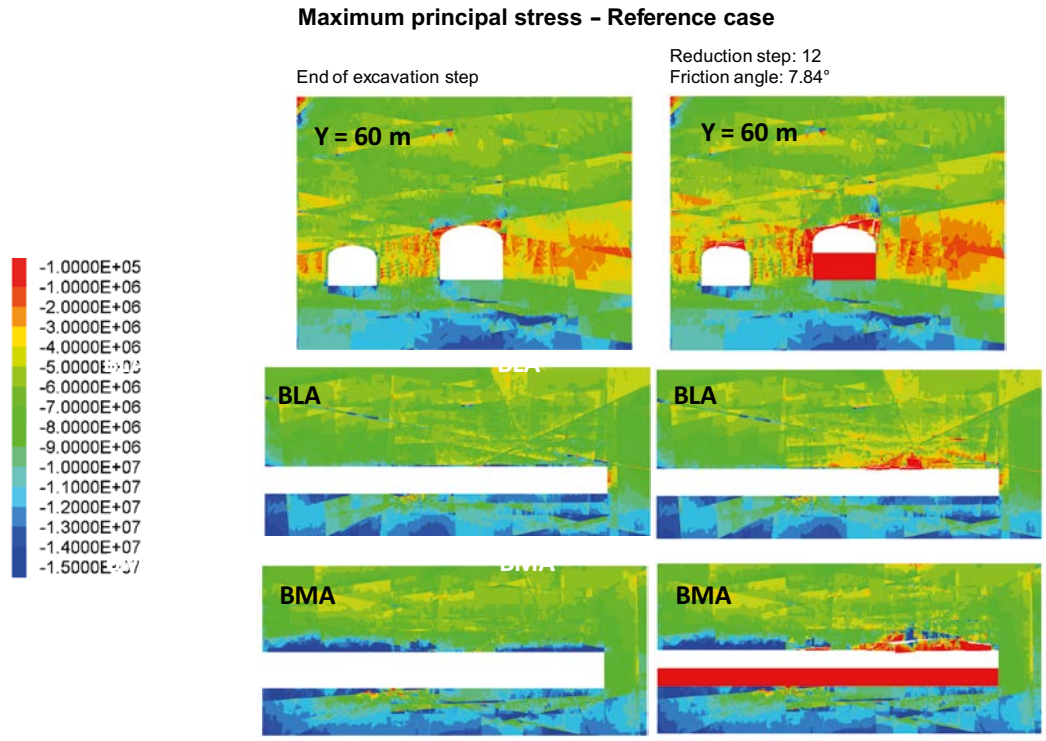

Figure 4-15. *Vertical cross-section contour plots of the maximum principal stress magnitude (in Pa) after excavation (left) and after the critical fracture friction angle has been reached (right) for the reference case. Cross section perpendicular to both caverns at Y = 60 m (upper) and two cross sections parallel to the caverns axis cutting through the middle of BLA cavern (middle) and BMA cavern (lower).*

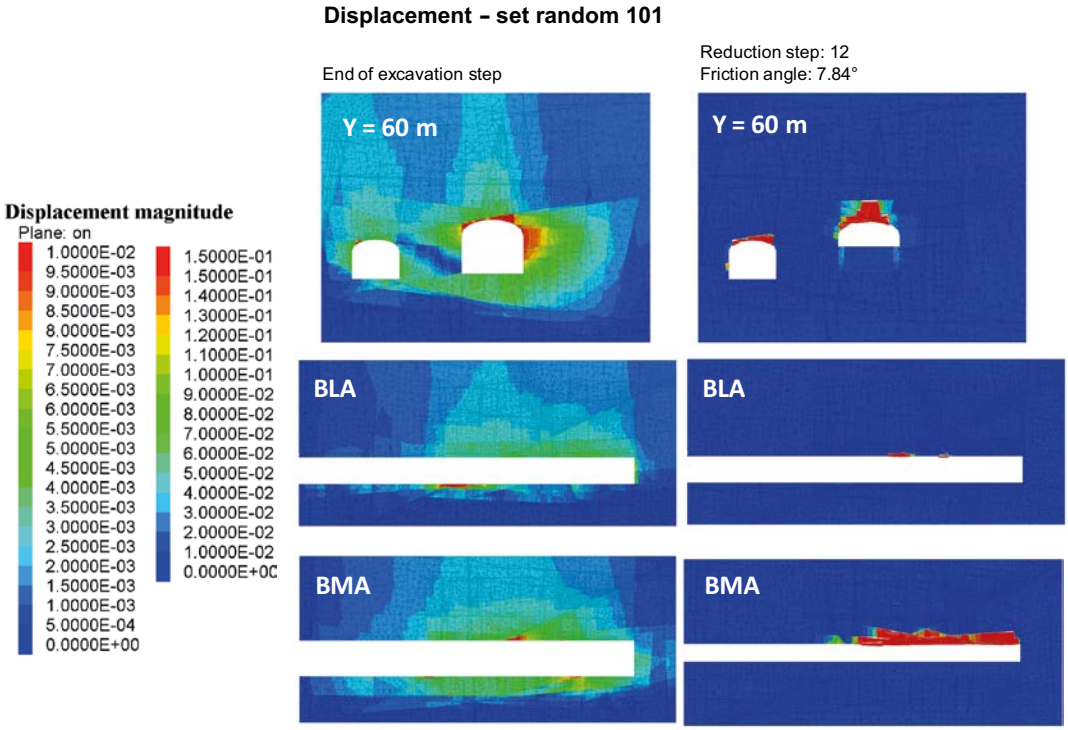

Figure 4-16. *Vertical cross-section contour plots of the displacements (in m) after excavation (left) and after the critical fracture friction angle has been reached (right) for case 101. Cross section perpendicular to both caverns at Y = 60 m (upper) and two cross sections parallel to the caverns axis cutting through the middle of BLA cavern (middle) and BMA cavern (lower). The legend to the left is for the excavation stage and the one to the right is for the critical fracture friction angle plots.*

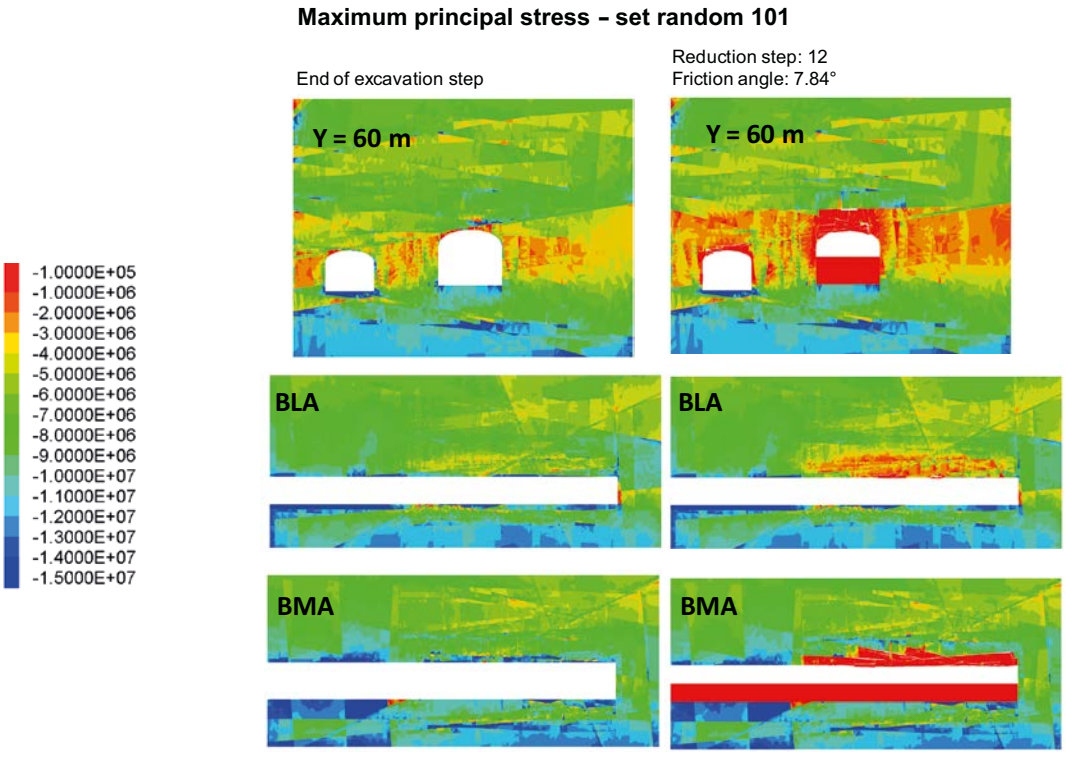

Figure 4-17. *Vertical cross-section contour plots of the maximum principal stress magnitude (in Pa) after excavation (left) and after the critical fracture friction angle has been reached (right) for case 101. Cross section perpendicular to both caverns at Y = 60 m (upper) and two cross sections parallel to the caverns axis cutting through the middle of BLA cavern (middle) and BMA cavern (lower).*

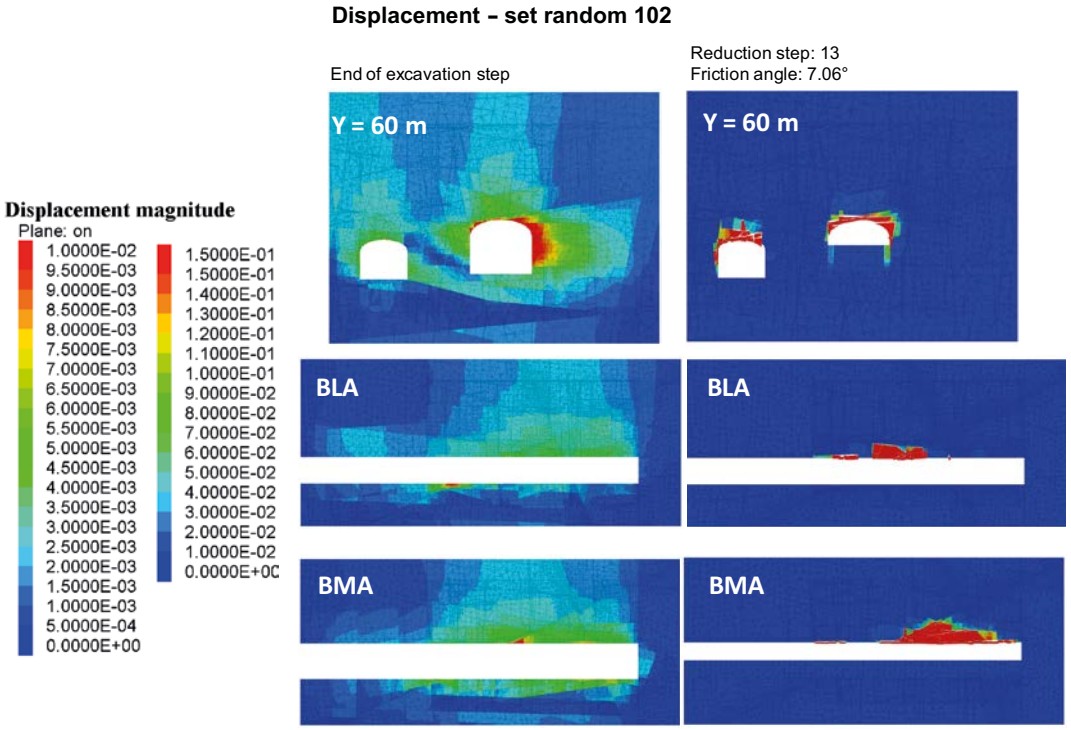

Figure 4-18. *Vertical cross-section contour plots of the displacements (in m) after excavation (left) and after the critical fracture friction angle has been reached (right) for case 102. Cross section perpendicular to both caverns at Y = 60 m (upper) and two cross sections parallel to the caverns axis cutting through the middle of BLA cavern (middle) and BMA cavern (lower). The legend to the left is for the excavation stage and the one to the right is for the critical fracture friction angle plots.*

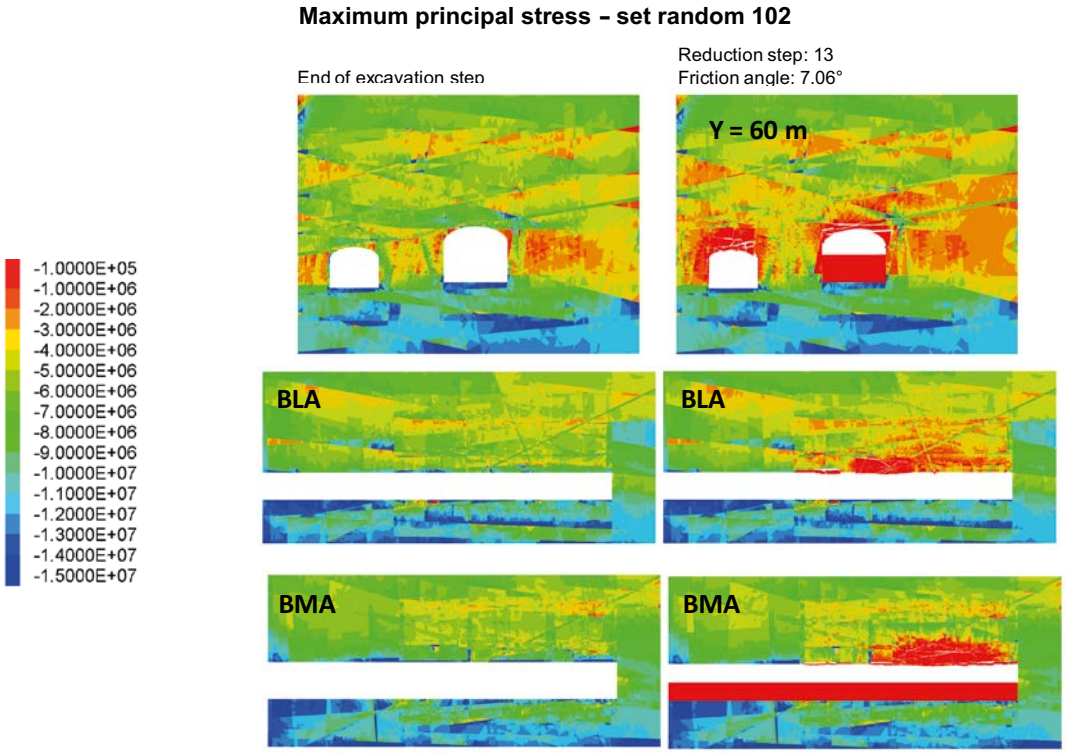

Figure 4-19. *Vertical cross-section contour plots of the maximum principal stress magnitude (in Pa) after excavation (left) and after the critical fracture friction angle has been reached (right) for case 102. Cross section perpendicular to both caverns at Y = 60 m (upper) and two cross sections parallel to the caverns axis cutting through the middle of BLA cavern (middle) and BMA cavern (lower).*

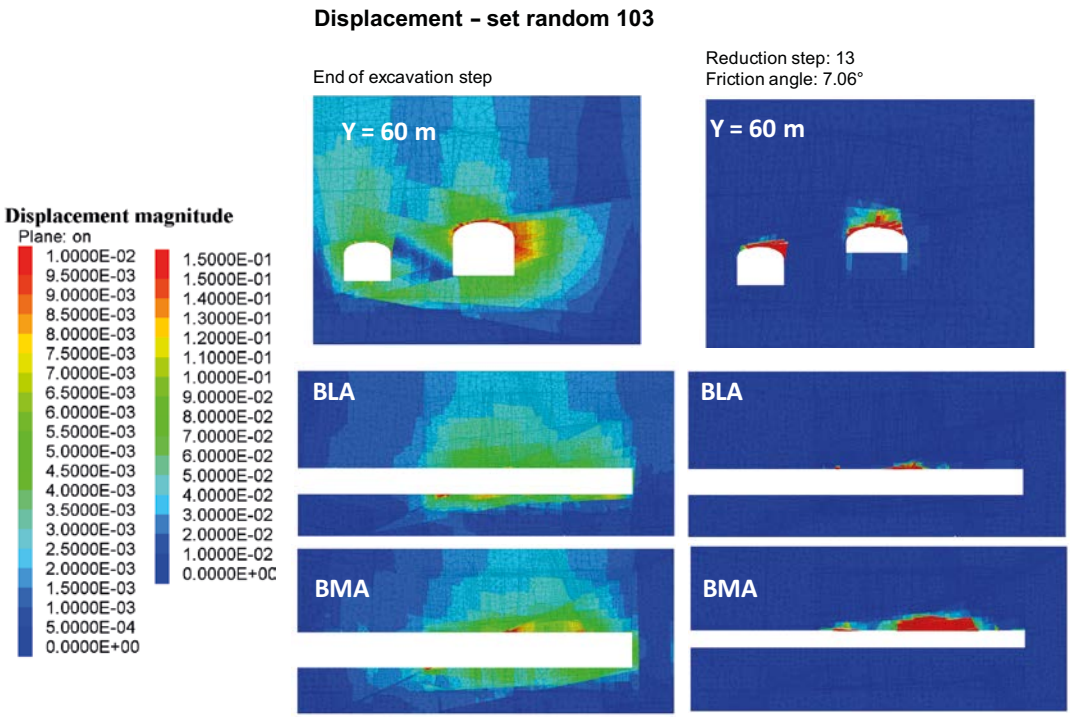

Figure 4-20. *Vertical cross-section contour plots of the displacements (in m) after excavation (left) and after the critical fracture friction angle has been reached (right) for case 103. Cross section perpendicular to both caverns at Y = 60 m (upper) and two cross sections parallel to the caverns axis cutting through the middle of BLA cavern (middle) and BMA cavern (lower). The legend to the left is for the excavation stage and the one to the right is for the critical fracture friction angle plots.*

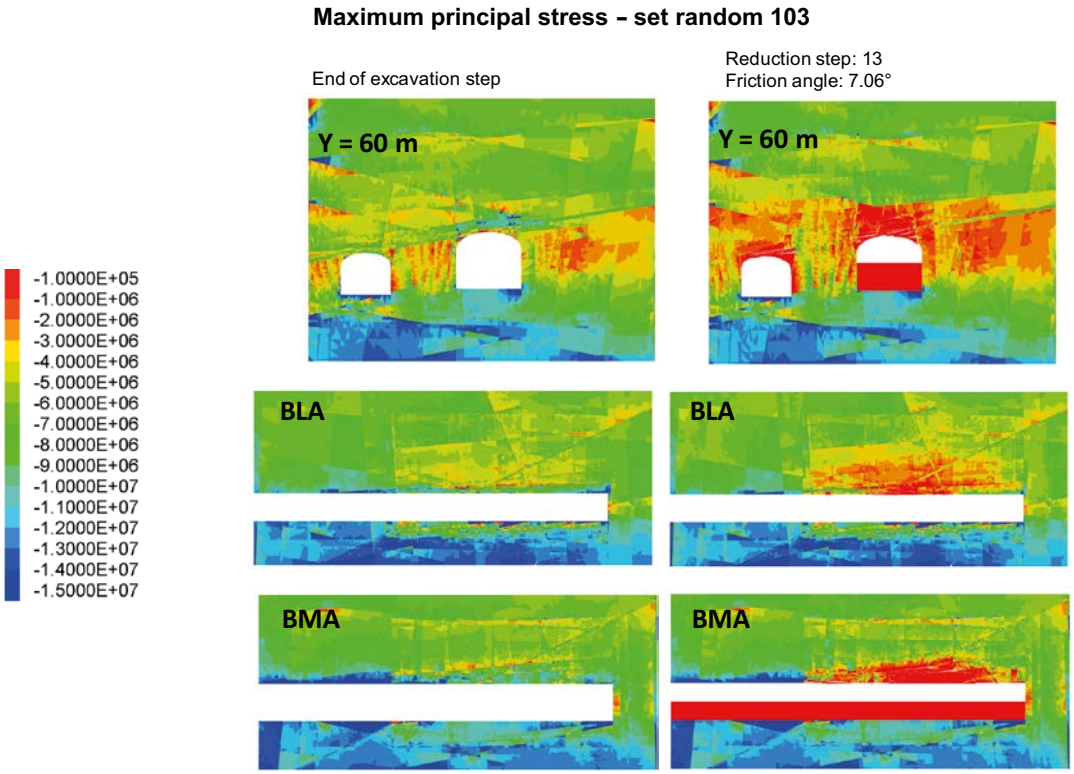

Figure 4-21. *Vertical cross-section contour plots of the maximum principal stress magnitude (in Pa) after excavation (left) and after the critical fracture friction angle has been reached (right) for case 103. Cross section perpendicular to both caverns at Y = 60 m (upper) and two cross sections parallel to the caverns axis cutting through the middle of BLA cavern (middle) and BMA cavern (lower).*

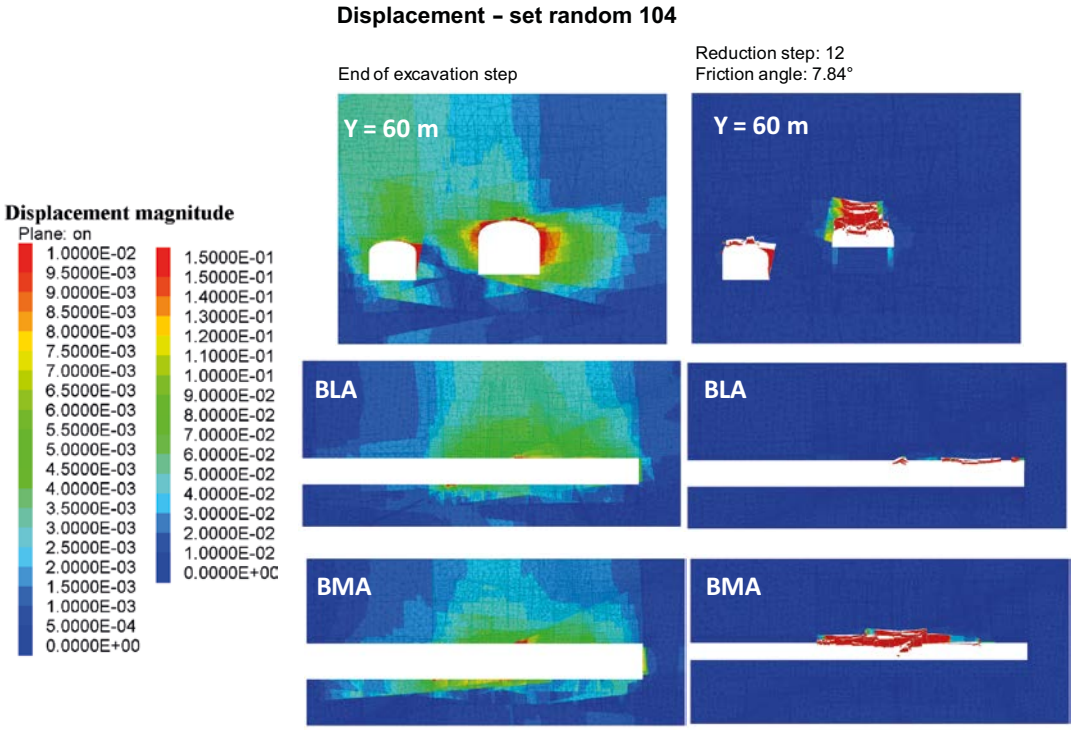

Figure 4-22. *Vertical cross-section contour plots of the displacements (in m) after excavation (left) and after the critical fracture friction angle has been reached (right) for case 104. Cross section perpendicular to both caverns at Y = 60 m (upper) and two cross sections parallel to the caverns axis cutting through the middle of BLA cavern (middle) and BMA cavern (lower). The legend to the left is for the excavation stage and the one to the right is for the critical fracture friction angle plots.*

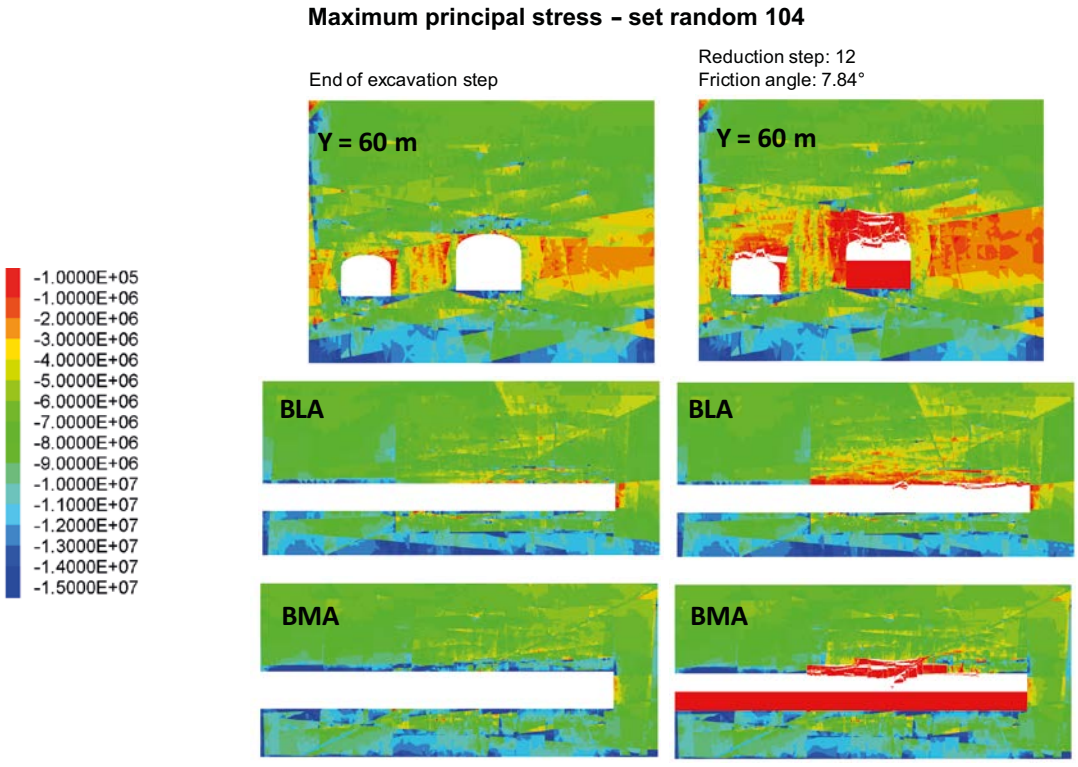

Figure 4-23. *Vertical cross-section contour plots of the maximum principal stress magnitude (in Pa) after excavation (left) and after the critical fracture friction angle has been reached (right) for case 104. Cross section perpendicular to both caverns at Y = 60 m (upper) and two cross sections parallel to the caverns axis cutting through the middle of BLA cavern (middle) and BMA cavern (lower).*

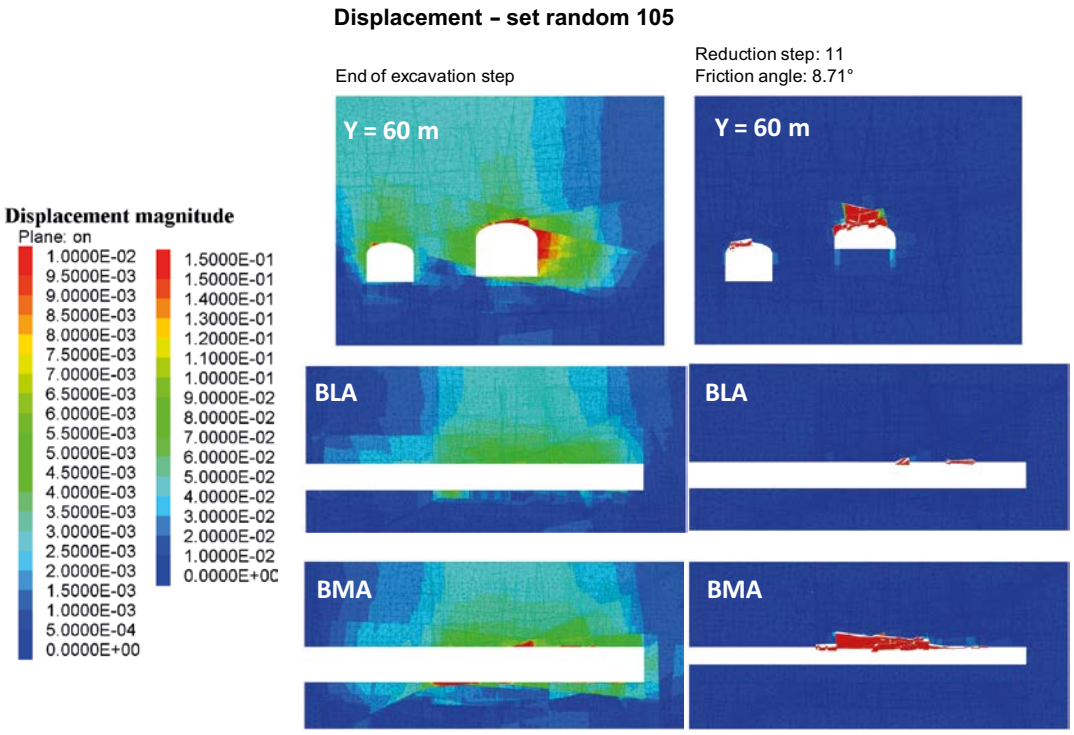

Figure 4-24. *Vertical cross-section contour plots of the displacements (in m) after excavation (left) and after the critical fracture friction angle has been reached (right) for case 105. Cross section perpendicular to both caverns at Y = 60 m (upper) and two cross sections parallel to the caverns axis cutting through the middle of BLA cavern (middle) and BMA cavern (lower). The legend to the left is for the excavation stage and the one to the right is for the critical fracture friction angle plots.*

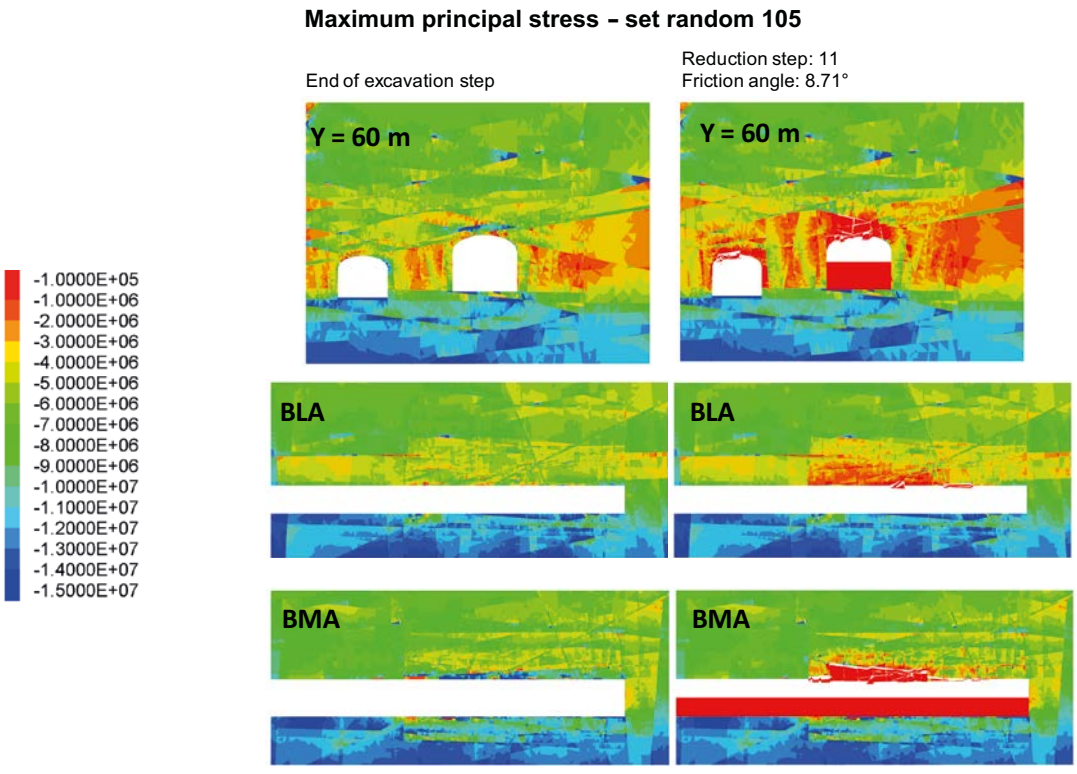

Figure 4-25. *Vertical cross-section contour plots of the maximum principal stress magnitude (in Pa) after excavation (left) and after the critical fracture friction angle has been reached (right) for case 105. Cross section perpendicular to both caverns at Y = 60 m (upper) and two cross sections parallel to the caverns axis cutting through the middle of BLA cavern (middle) and BMA cavern (lower).*

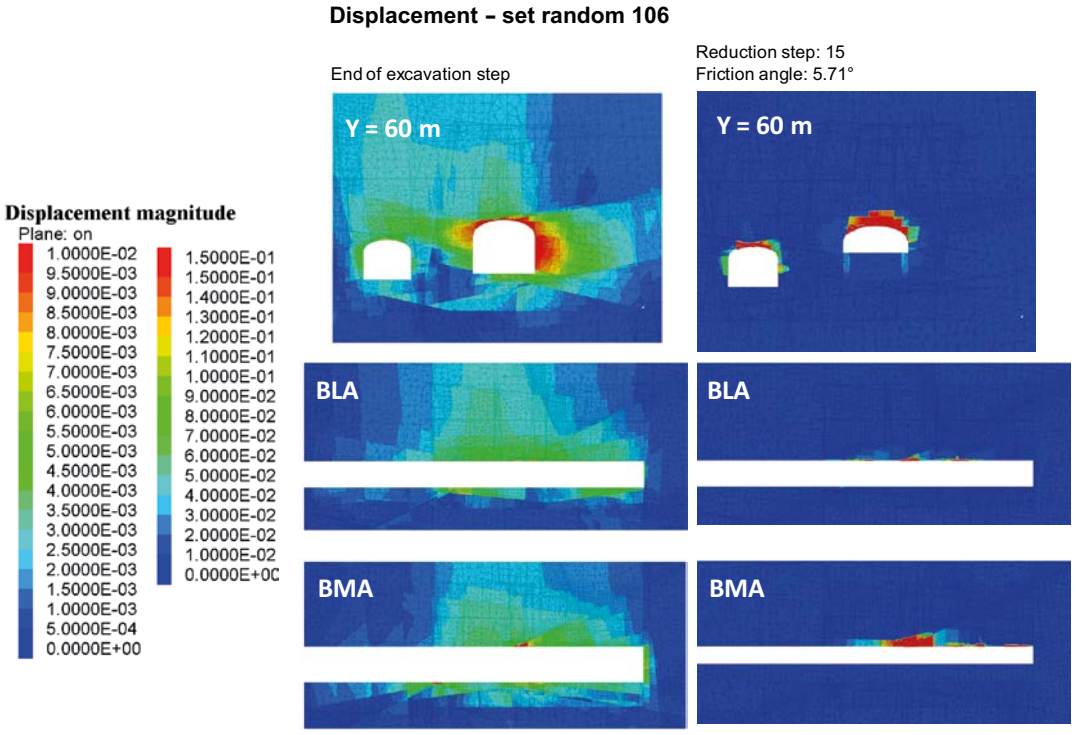

Figure 4-26. *Vertical cross-section contour plots of the displacements (in m) after excavation (left) and after the critical fracture friction angle has been reached (right) for case 106. Cross section perpendicular to both caverns at Y = 60 m (upper) and two cross sections parallel to the caverns axis cutting through the middle of BLA cavern (middle) and BMA cavern (lower). The legend to the left is for the excavation stage and the one to the right is for the critical fracture friction angle plots.*

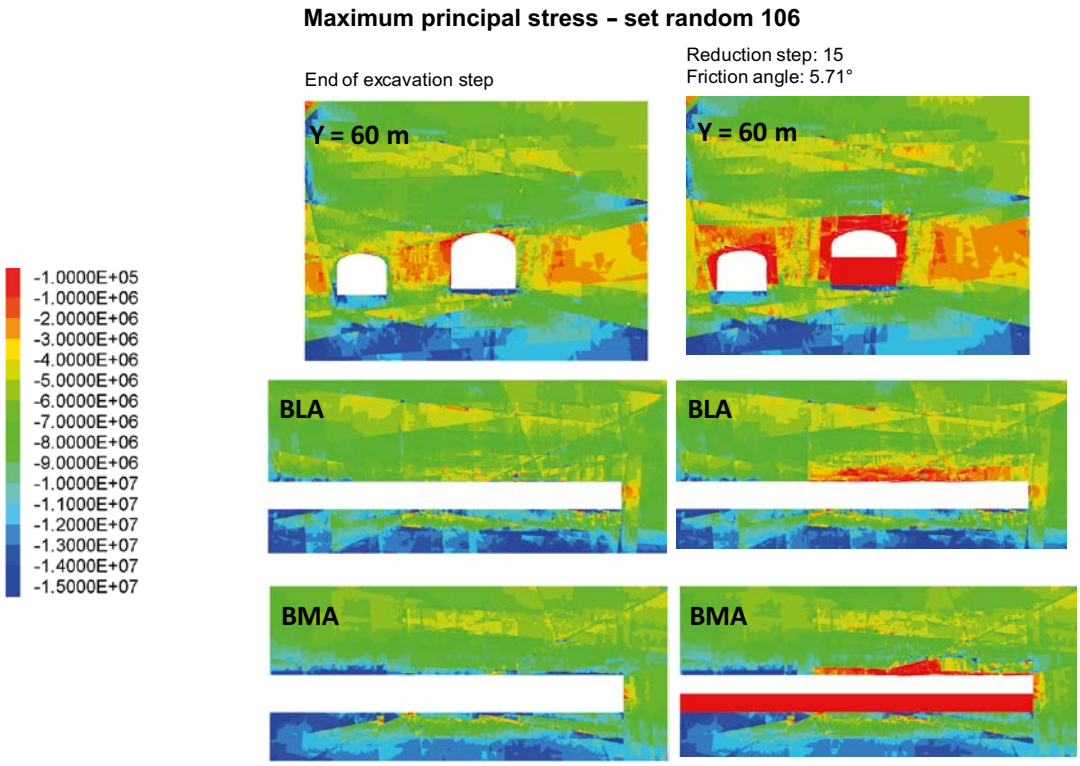

Figure 4-27. *Vertical cross-section contour plots of the maximum principal stress magnitude (in Pa) after excavation (left) and after the critical fracture friction angle has been reached (right) for case 106. Cross section perpendicular to both caverns at Y = 60 m (upper) and two cross sections parallel to the caverns axis cutting through the middle of BLA cavern (middle) and BMA cavern (lower).*

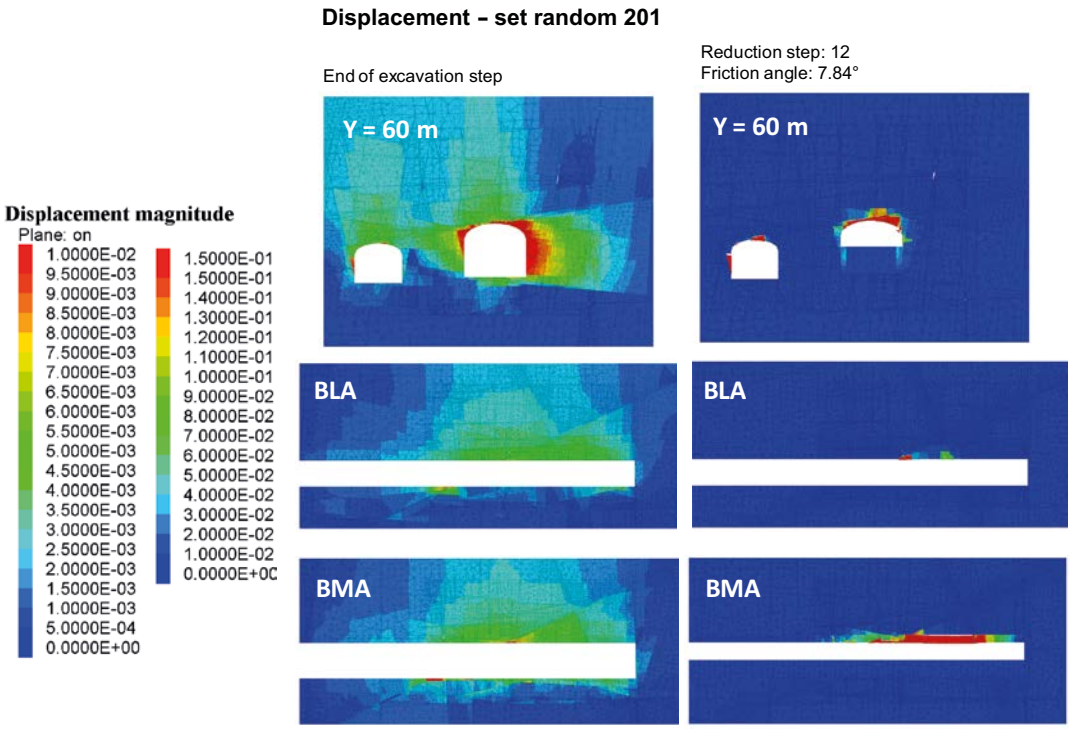

Figure 4-28. *Vertical cross-section contour plots of the displacements (in m) after excavation (left) and after the critical fracture friction angle has been reached (right) for case 201. Cross section perpendicular to both caverns at Y = 60 m (upper) and two cross sections parallel to the caverns axis cutting through the middle of BLA cavern (middle) and BMA cavern (lower). The legend to the left is for the excavation stage and the one to the right is for the critical fracture friction angle plots.*

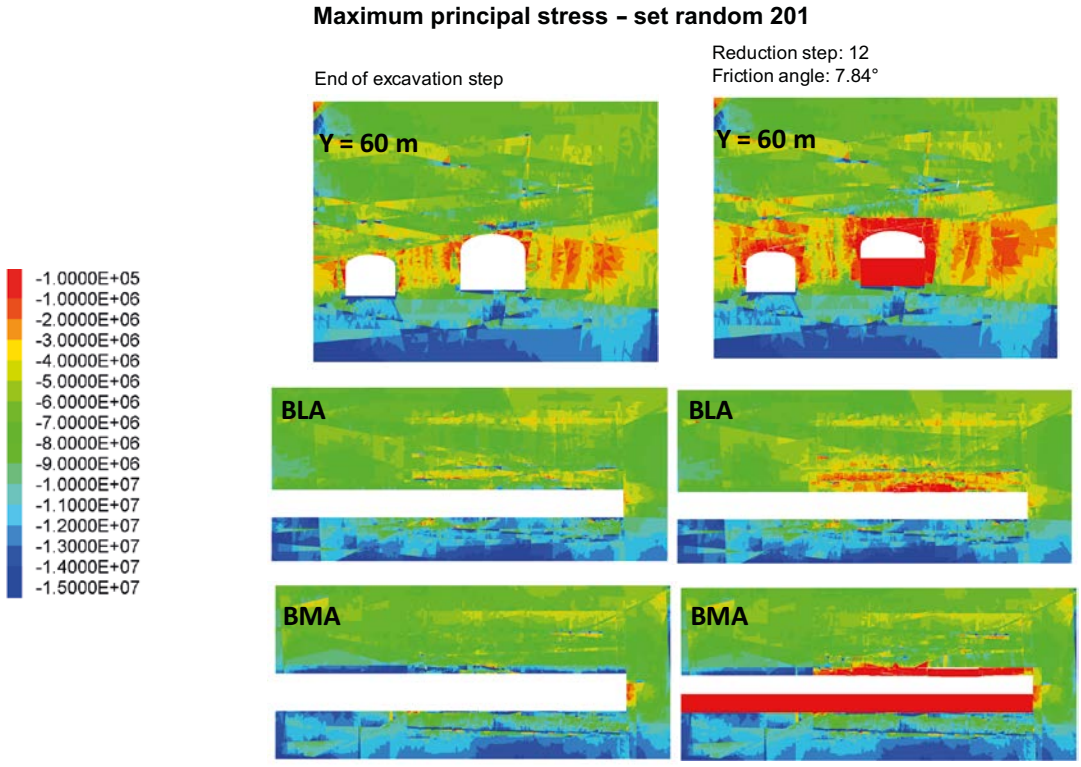

Figure 4-29. *Vertical cross-section contour plots of the maximum principal stress magnitude (in Pa) after excavation (left) and after the critical fracture friction angle has been reached (right) for case 201. Cross section perpendicular to both caverns at Y = 60 m (upper) and two cross sections parallel to the caverns axis cutting through the middle of BLA cavern (middle) and BMA cavern (lower).*

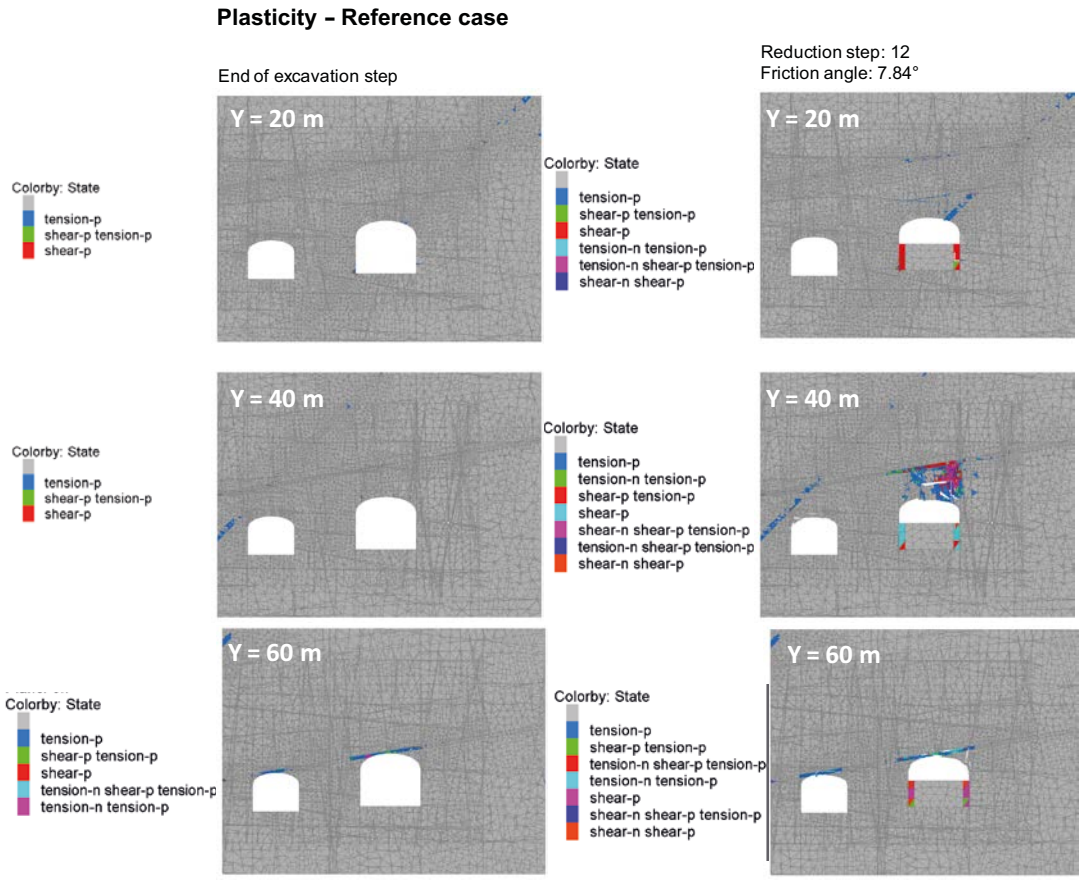

Figure 4-30. *Vertical cross-section plots of the plasticity after excavation (left) and after the critical fracture friction angle has been reached (right) for the reference case. Cross section perpendicular to both caverns at Y = 20 m (upper), Y = 40 m (middle) and Y = 60 m (lower).*

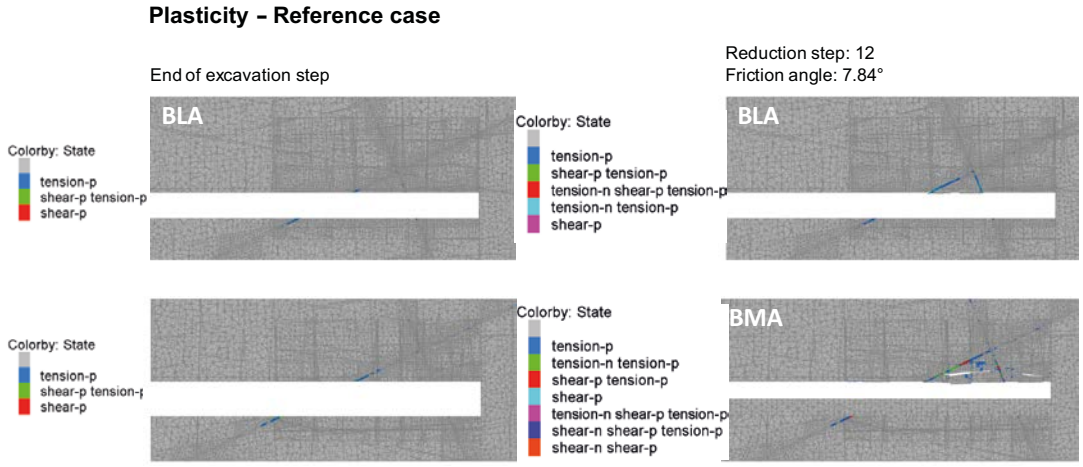

Figure 4-31. *Vertical cross-section plots of the plasticity after excavation (left) and after the critical fracture friction angle has been reached (right) for the reference case. Two cross sections parallel to the caverns axis cutting through the middle of BLA cavern (middle) and BMA cavern (lower).*

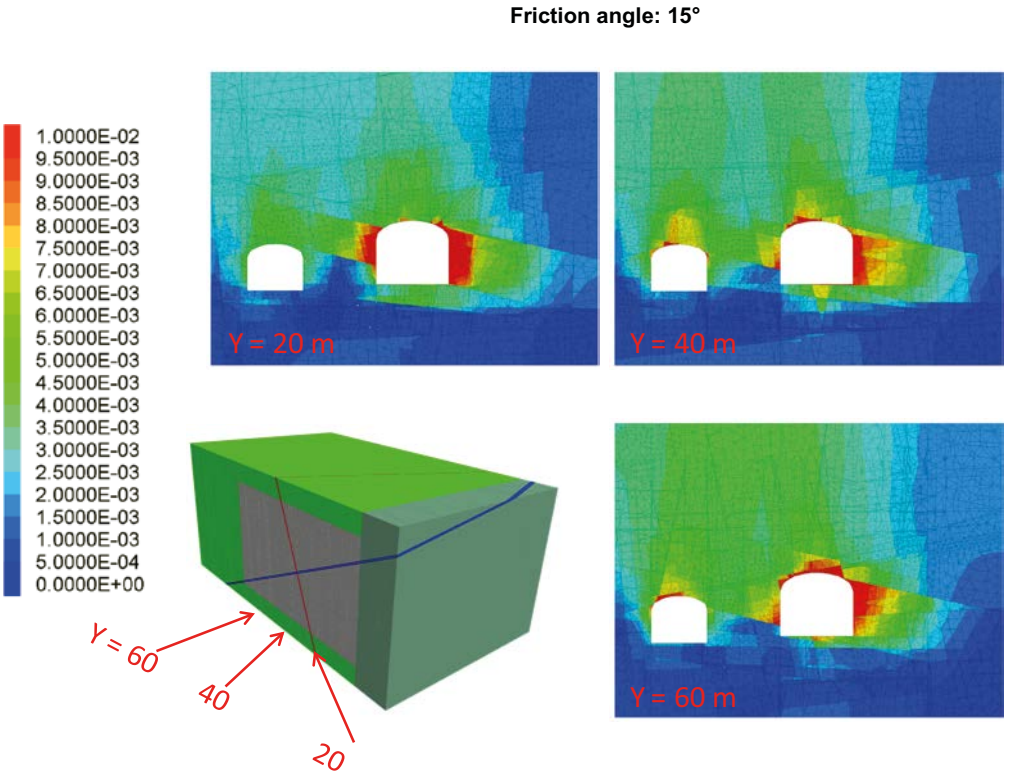

Figure 4-32. *Vertical cross-section contour plots of the displacements (in m) after excavation for case 105 (Figure 4-6). Cross section perpendicular to both caverns at Y = 20 m, Y = 40 m and Y = 60 m.*

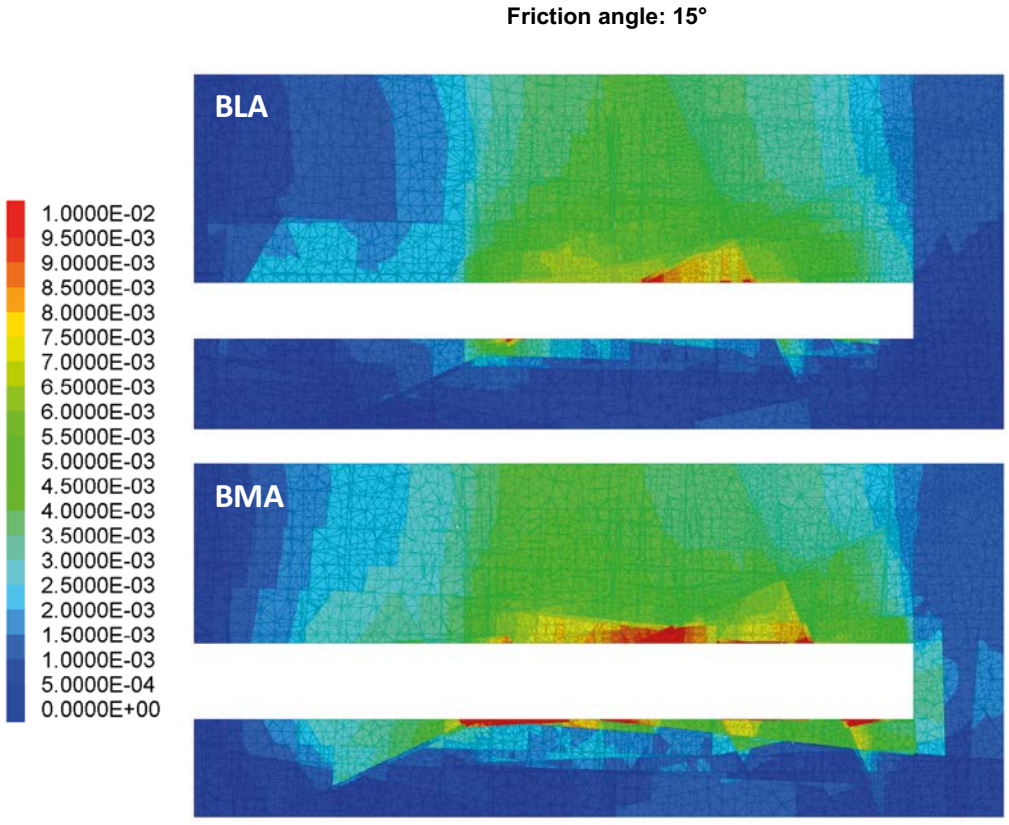

Figure 4-33. *Vertical cross-section contour plots of the displacements (in m) after excavation for case 105 (Figure 4-6). Two cross sections parallel to the caverns axis cutting through the middle of BLA cavern (upper) and BMA cavern (lower).*

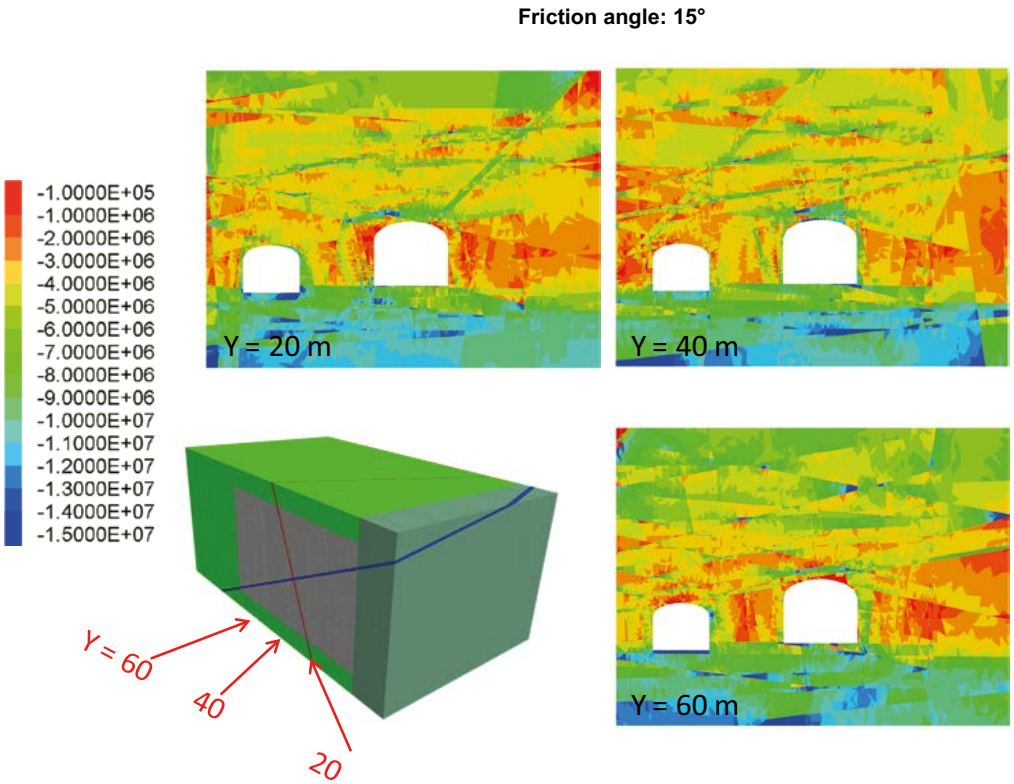

Figure 4-34. *Vertical cross-section contour plots of the maximum principal stress magnitude (in Pa) after excavation for case 105 (Figure 4-6). Cross section perpendicular to both caverns at Y = 20 m, Y = 40 m and Y = 60 m.*

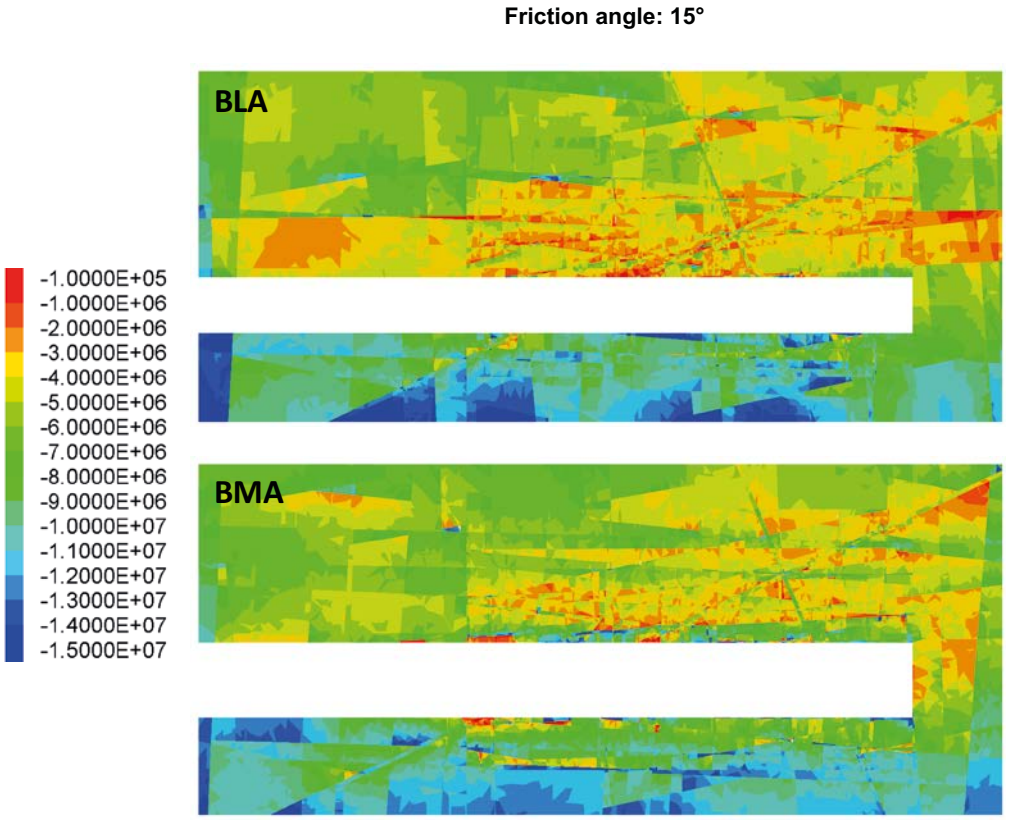

Figure 4-35. *Vertical cross-section contour plots of the maximum principal stress magnitude (in Pa) after excavation for case 105 (Figure 4-6). Two cross sections parallel to the caverns axis cutting through the middle of BLA cavern (upper) and BMA cavern (lower).*

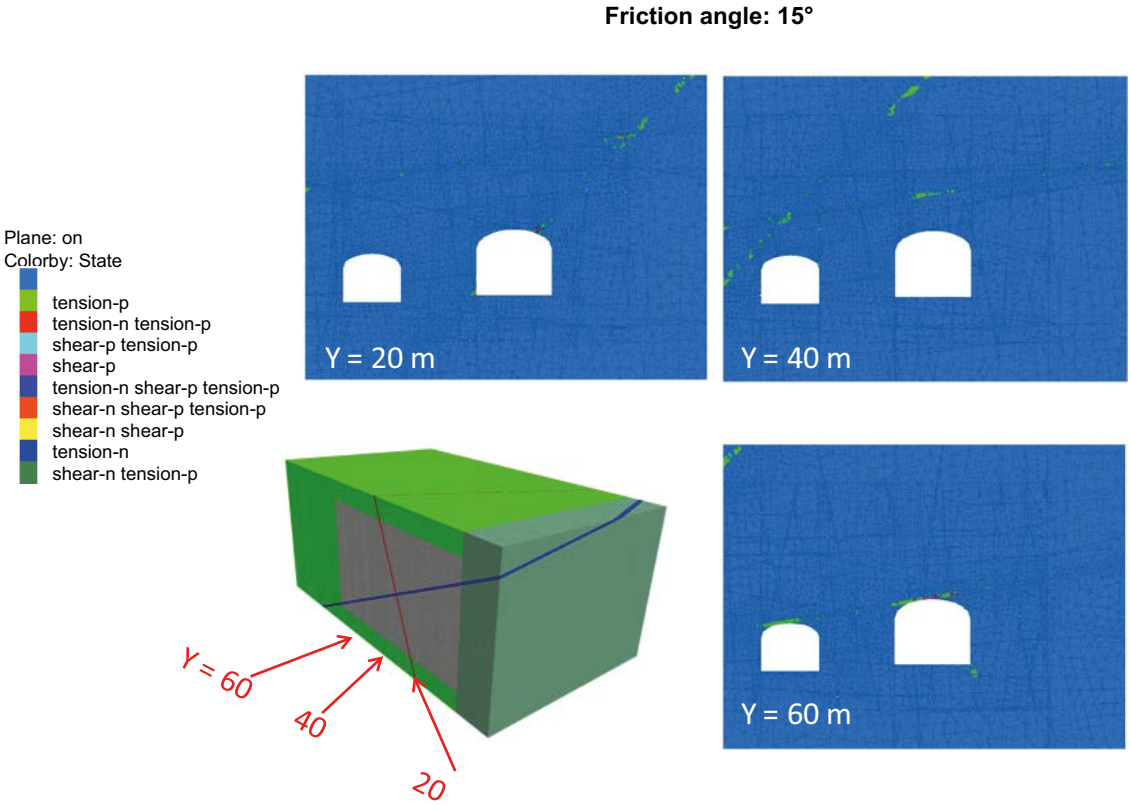

Figure 4-36. *Vertical cross-section contour plots of plasticity after excavation for case 105 (Figure 4-6). Cross section perpendicular to both caverns at Y = 20 m, Y = 40 m and Y = 60 m.*

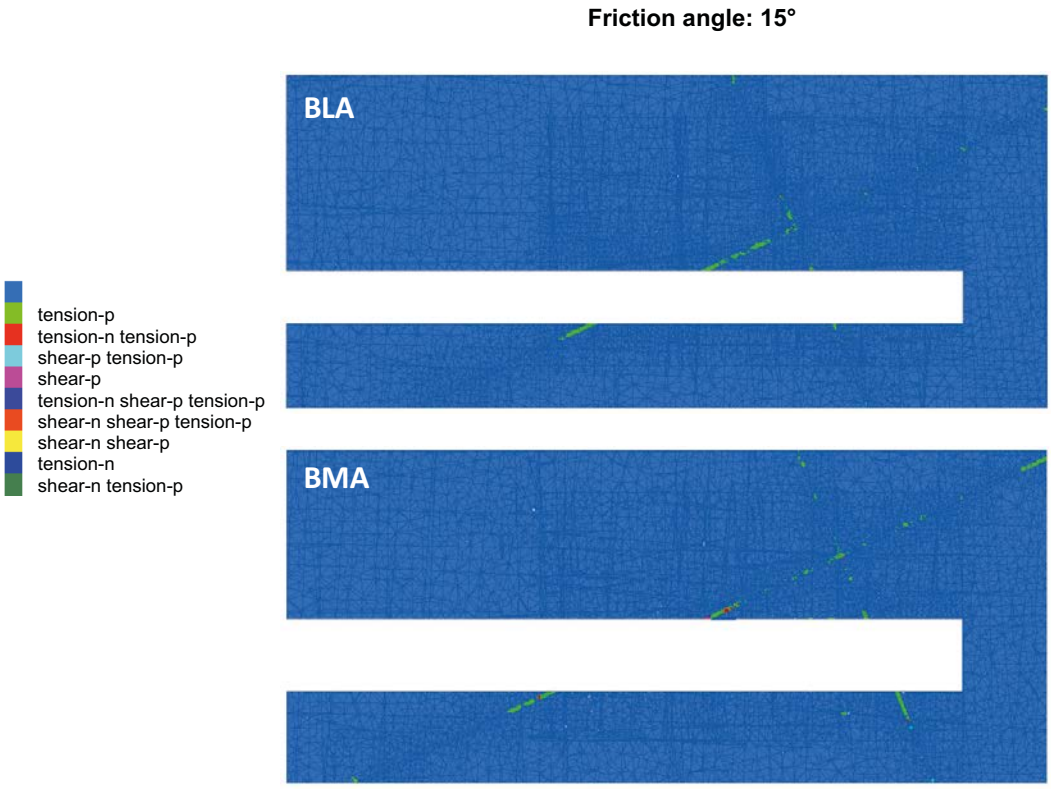

Figure 4-37. *Vertical cross-section contour plots of plasticity after excavation for case 105 (Figure 4-6). Two cross sections parallel to the caverns axis cutting through the middle of BLA cavern (upper) and BMA cavern (lower).*

4.2.2 Long term stability

The plots in Figure 4-14 to Figure 4-29 also contain, for comparison purposes, the final simulation state achieved once the friction in the fractures planes forming blocks in the vicinity of the caverns has been reduced to the critical fracture friction angle (the friction angle required for the fractures to slip). At this point, the first blocks around the caverns have begun to fall and the whole volume around them is becoming de-stressed. However, in order for the next layer of blocks surrounding the excavation boundaries to fall, the friction angle in the fracture planes that form them has to be reduced to a similar value as the one identified for the first layer of blocks to fall. This is consistent for all the simulation cases.

These results show the stress release caused by the reduction of the fracture friction angle in the roof and walls of the caverns due to fracture slip.

According to the simulation results, the critical friction angle necessary for blocks to begin falling ranges from 5.7° to 8.7° for the eight cases considered. This is comparable to the absolute worst case of residual friction angle (8°) from the world literature review presented in Section 2.4.3. What is more, it is well under 15–17°, which is the lowest value of residual friction angles expected at Forsmark **(**Section 2.4.3).

The displacement of the sand layer (2 m thickness) reaches in some cases a maximum of around 10 cm when blocks start to fall. The sand layer is compressed in horizontal direction and extended in the vertical direction. The stress in the concrete remains relatively small (<1MPa) during the fracture property reduction steps.

The results on plasticity presented in Figure 4-30 and Figure 4-31 for the reference DFN case show that plastification occurs first at the deformation zones and then develops within the intersection between the deformation zones. The sand fails in shear and reduces the stresses on the concrete. The concrete does not fail. The rest of the cases showed similar results.

As mentioned previously, a deformable rock block case with no standard deviation on the orientation of the fractures has been analyzed. In that case the BMA cavern was excavated considering the sand and concrete are already present during excavation as rock material. A “reference case” DFN run **(**Figure 4-5 was also run in a similar manner to be able to compare the results. The maximum displacements after excavation were ~ 1 cm for the run without standard deviation and ~ 3 cm for the reference case run. The critical fracture friction angles were 0.6° and 7.8° respectively. The later agrees well with the critical fracture friction angle derived when considering the sand and concrete explicitly (Figure 4-14 and Figure 4-15).

4.2.3 Sensitivity to in situ stress

To investigate the sensitivity to in situ stress a simulation with isotropic (hydrostatic) stress was run with the DFN generated with the random seed number 105. The results of these simulations indicate that the caverns are stable after excavation without reinforcement and become unstable (blocks begin to fall) when the fracture friction angle is reduced to 18.2°. The results are presented in Appendix 1.

4.2.4 Reduction of the fracture friction angle until the caverns are filled with rock blocks (rigid block case)

The last objective was to assess if the caverns would be self-supporting if it is possible to artificially reduce the fracture friction angle in a region around the two caverns to a value low enough to cause the caverns to become full of rock blocks. In this case the “reference case” DFN model **(**Figure 4-5) was run in rigid block mode. This means stress only develops in the fractures as the blocks are rigid and therefore do not deform. This makes the simulation time much faster. The geometry in Figure 4-3 was used for this model where the model extends up to the surface.

The results from the calculations with the rigid block model show that the blocks start to fall in at a reduced friction angle equal to 5.7°, see Figure 4-38 to Figure 4-41. It is also seen that the zone of the loosening rock mass progresses as the zone with a reduced friction angle below 5.7° increases. This continues until the caverns are filled with blocks, see Figure 4-42 to Figure 4-45. The height of the zone with a loosening rock mass reaches up to 34 m above the original cavern roof. At this stage, the deformation at the rock surface is approximately 3.5 cm, see Figure 4-46.

The calculations also show that the pillar is de-stressed when the loosening zones above each cavern merge together. This enables shear displacements in horizontal persistent fractures through the pillar, see Figure 4-44. However, the normal displacements are small, see Figure 4-45.

However, when the results are interpreted, is should be emphasized that the reduced friction angle in the fractures that is required in order to initiate this loosening of the rock mass is unrealistically low. The modeled scenario is therefore not realistic.

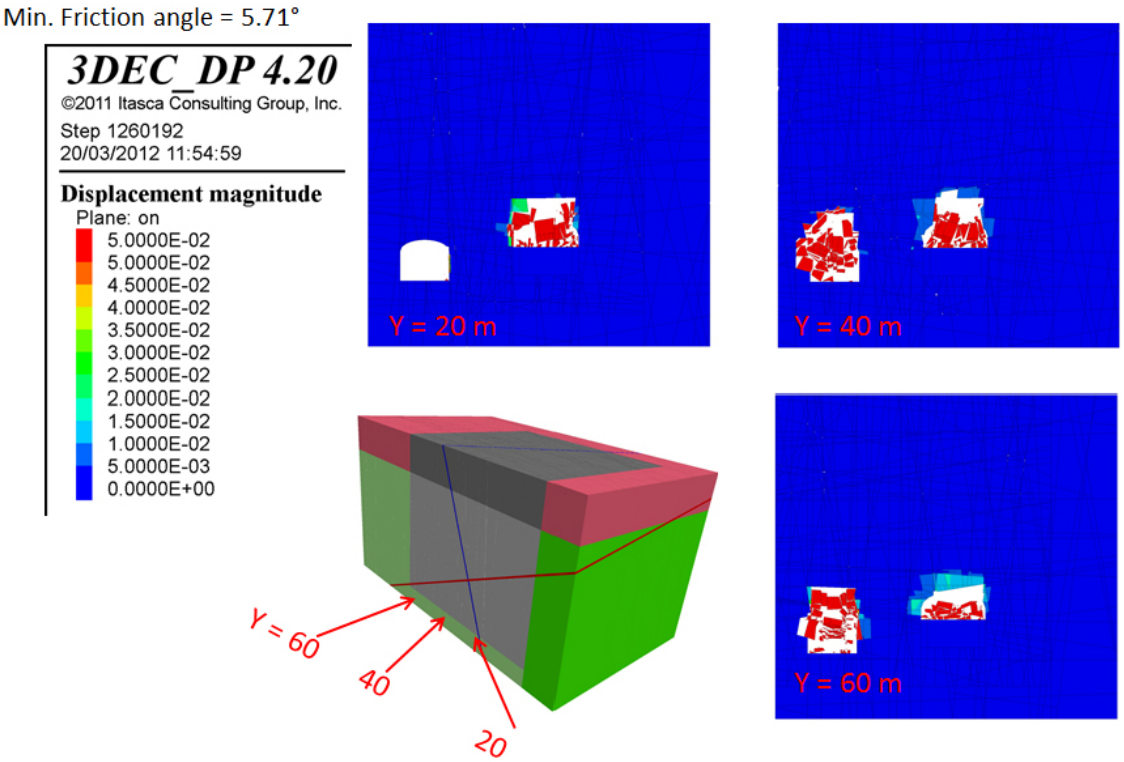

Figure 4-38. *Vertical cross-section contour plots of the displacements (in m) for the "reference case" rigid block model (Figure 4-6) at reduction step 15. Cross section perpendicular to both caverns at Y = 20 m, Y = 40 m and Y = 60 m.*

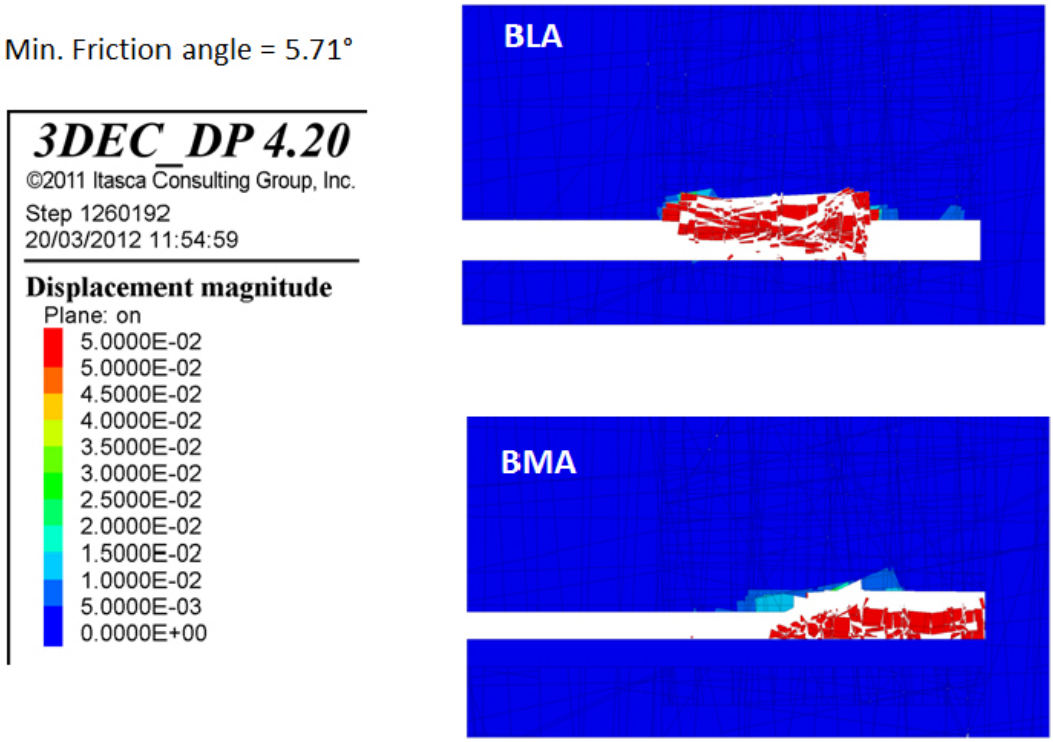

Figure 4-39. *Vertical cross-section contour plots of the displacements (in m) for the "reference case" rigid block model (Figure 4-6) at reduction step 15. Two cross sections parallel to the caverns axis cutting through the middle of BLA cavern (upper) and BMA cavern (lower).*

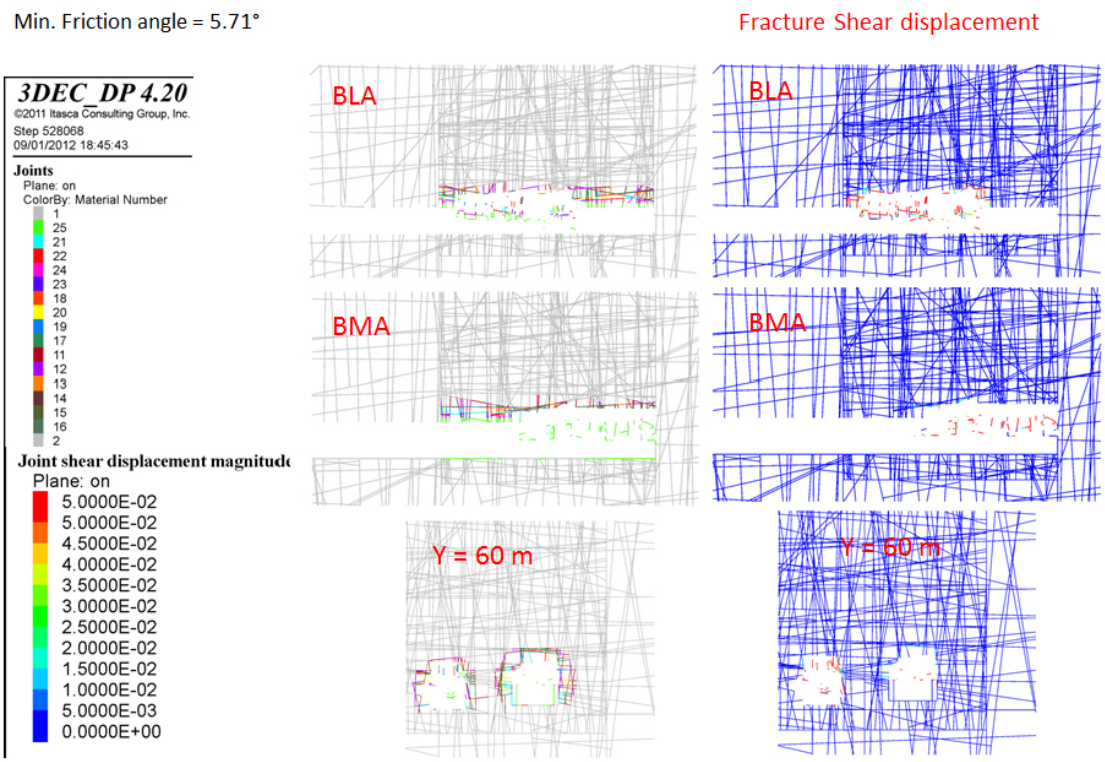

Figure 4-40. *Vertical cross-section plots of the fracture shear displacements (in m) for the "reference case" rigid block model (Figure 4-6) at reduction step 15. Cross section perpendicular to both caverns at Y = 60 m (lower) and two cross sections parallel to the caverns axis cutting through the middle of BLA cavern (upper) and BMA cavern (middle). The plot also shows the extent of the fracture property reduction zone (left).*

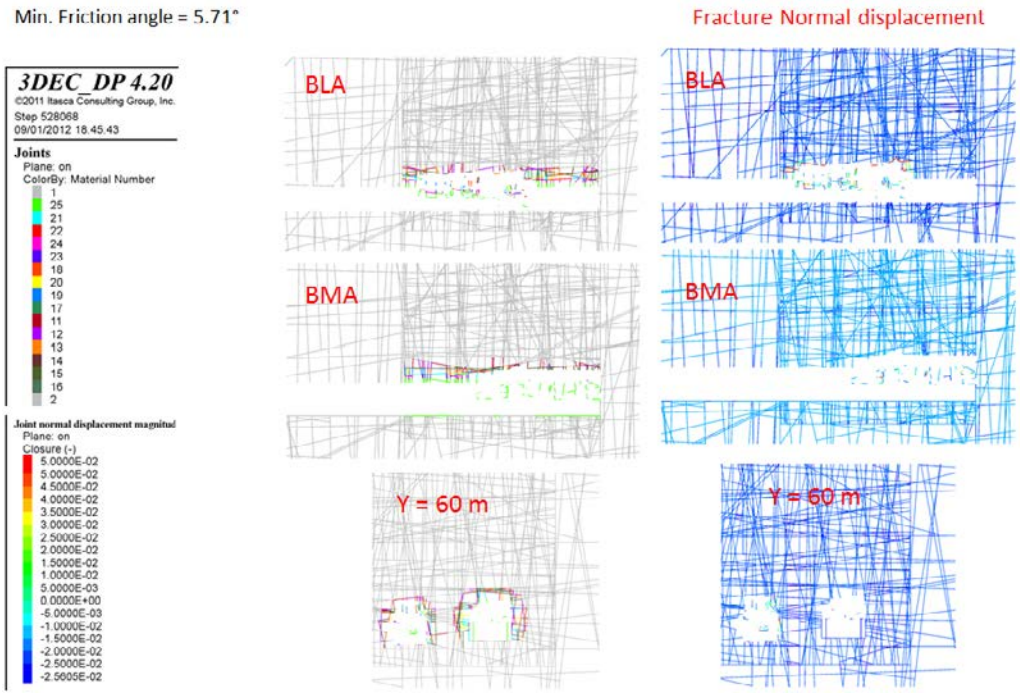

Figure 4-41. *Vertical cross-section contour plots of the fracture normal displacements (in m) (right) for the "reference case" rigid block model (Figure 4-6) at reduction step 15. Cross section perpendicular to both caverns at Y = 60 m (lower) and two cross sections parallel to the caverns axis cutting through the middle of BLA cavern (upper) and BMA cavern (middle). The plot also shows the extent of the fracture property reduction zone (left).*

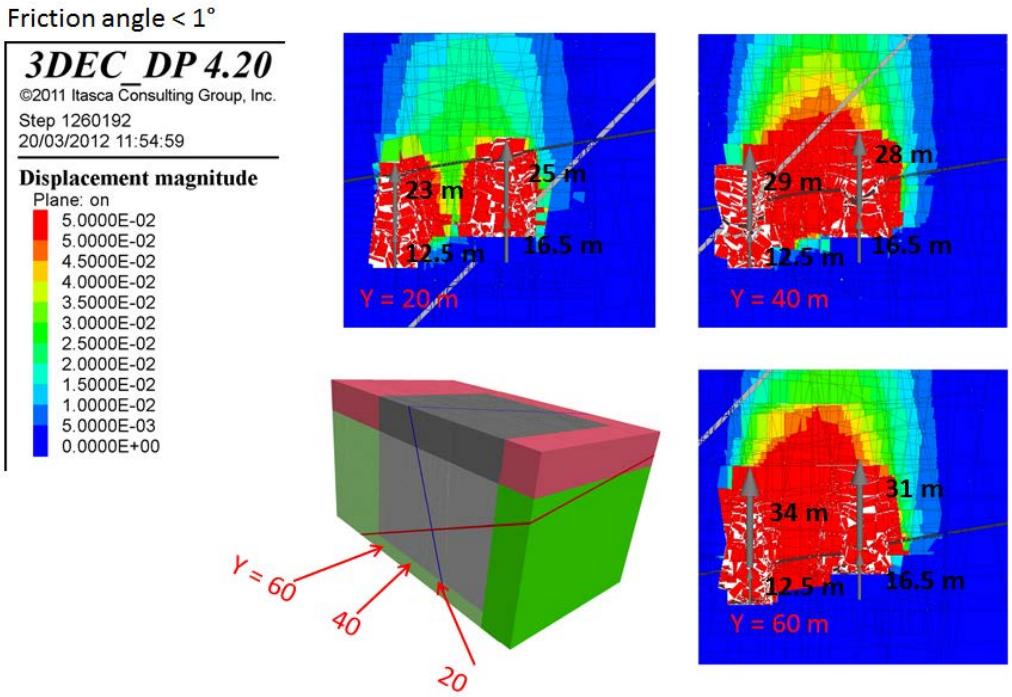

Figure 4-42. *Vertical cross-section contour plots of the displacements (in m) for the "reference case" rigid block model (Figure 4-6) at reduction step 36. Cross section perpendicular to both caverns at Y = 20 m, Y = 40 m and Y = 60 m.*

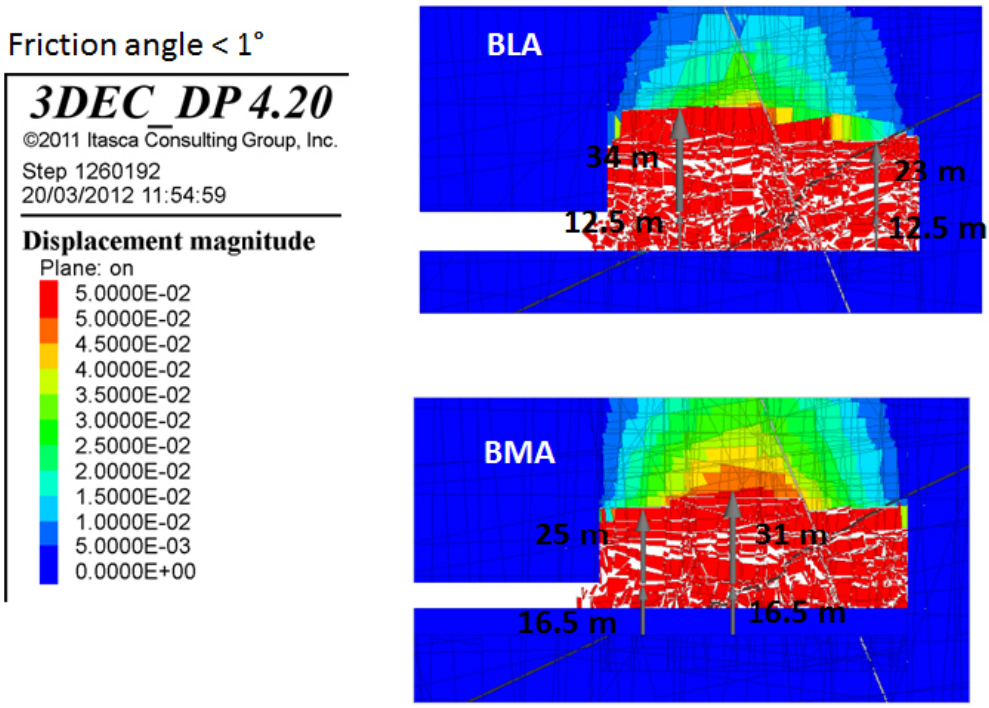

Figure 4-43. *Vertical cross-section contour plots of the displacements (in m) for the "reference case" rigid block model (Figure 4-6) at reduction step 36. Two cross sections parallel to the caverns axis cutting through the middle of BLA cavern (upper) and BMA cavern (lower).*

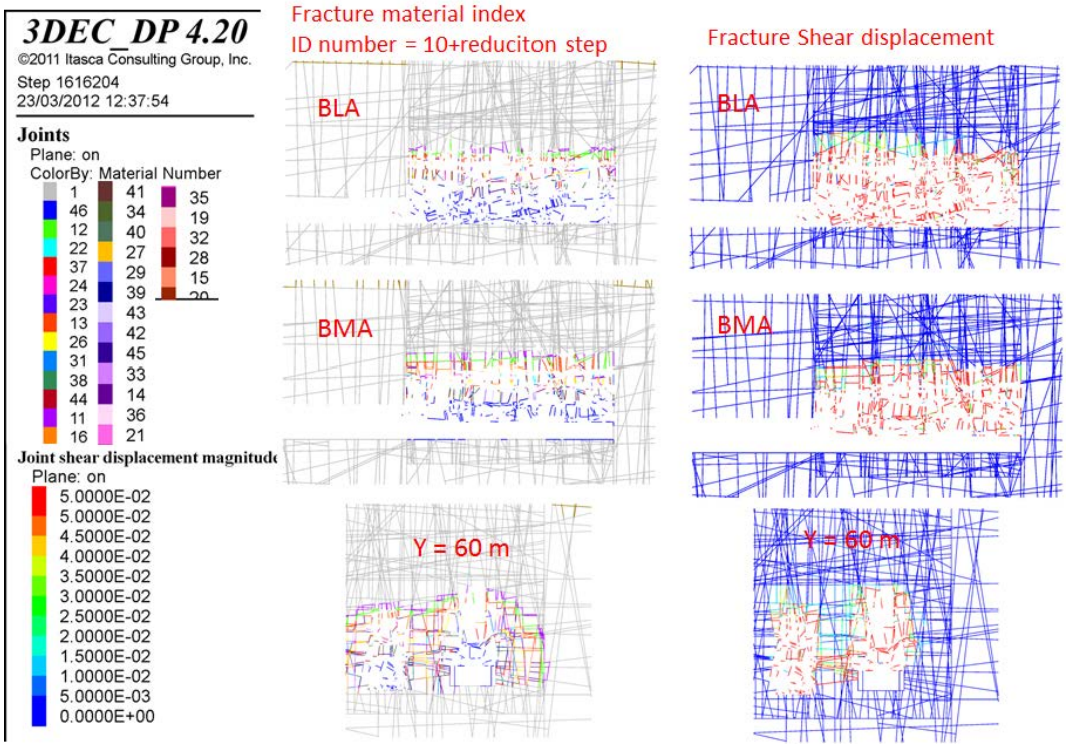

Figure 4-44. *Vertical cross-section plots of the fracture shear displacements (in m) for the "reference case" rigid block model (Figure 4-6) at reduction step 36. Cross section perpendicular to both caverns at Y = 60 m (lower) and two cross sections parallel to the caverns axis cutting through the middle of BLA cavern (upper) and BMA cavern (middle). The plot also shows the extent of the fracture property reduction zone (left).*

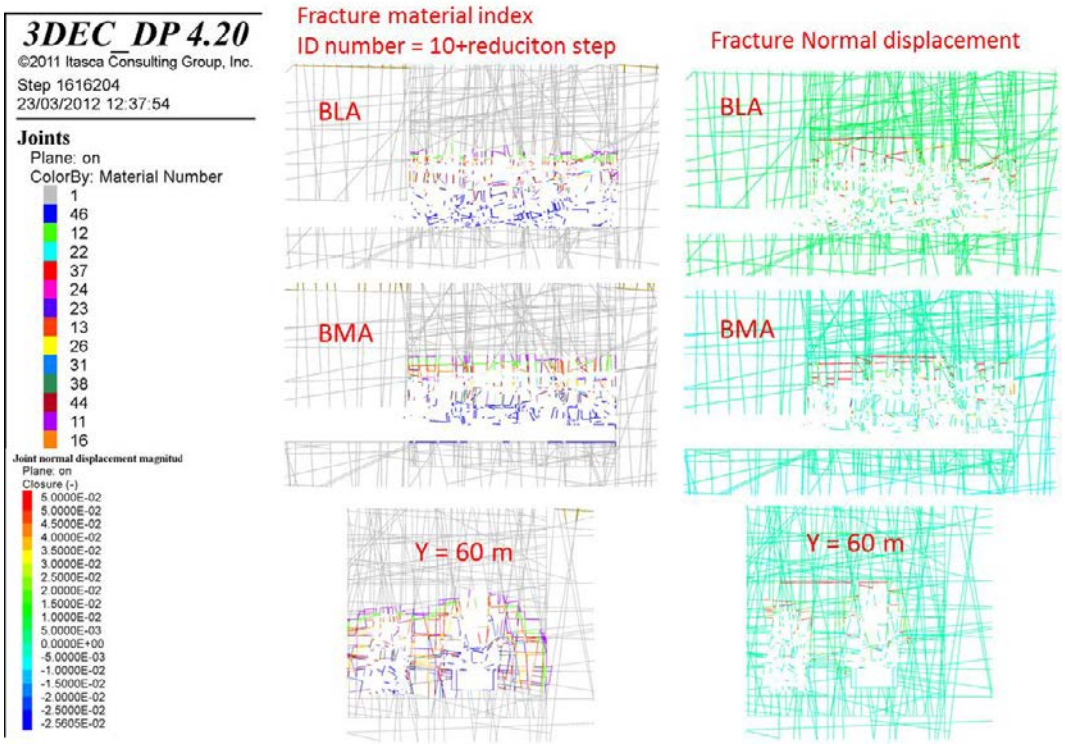

Figure 4-45. *Vertical cross-section contour plots of the fracture normal displacements (in m) (right) for the "reference case" rigid block model (Figure 4-6) at reduction step 36. Cross section perpendicular to both caverns at Y = 60 m (lower) and two cross sections parallel to the caverns axis cutting through the middle of BLA cavern (upper) and BMA cavern (middle). The plot also shows the extent of the fracture property reduction zone (left).*

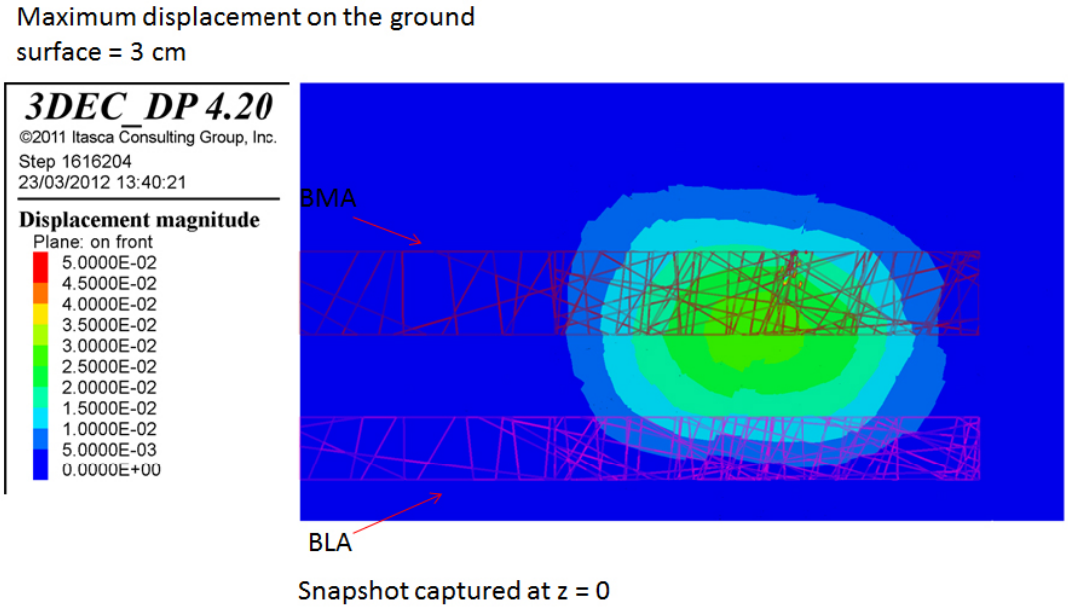

Figure 4-46. *Displacements (in m) at the rock surface (right) for the "reference case" rigid block model (Figure 4-6) at reduction step 36..*

5 Summary and conclusions

A random fracture generator has been used to construct 3DEC models that capture the statistics of the mapped fractures at the studied caverns at SFR. The results from the study show that the block stability is governed by the fracture geometry, the residual friction angle in the fractures and the in situ stresses.

A number of assumptions and simplifications have been used in this study. These are summarized in the following points:

- The fractures included in the model were all assumed to have infinite length. This is considered to be conservative.
- A fracture shear dilation angle of zero degrees was considered in all the simulations. This is considered to be conservative.
- No pore pressure was considered in the fractures. The effect of this assumption in the overall stability of the caverns is complex to predict. Pore pressure would decrease the shear strength of the fractures but would also give some supporting pressure at the excavation boundaries. To include fracture pore pressure in hydro-mechanical coupled calculations requires major computational time. Instead the analysed case was purely a mechanical calculation case, where very low friction angels are assumed and the decrease in shear strength due to pore pressure, is indirectly addressed.

Additionally, the effect of uncertainty in in situ stress has been considered by simulating a case with isotropic (hydrostatic) in situ stress (see Appendix 1). This case is considered as a completely unrealistic worst case scenario in terms of in situ stress.

The caverns remain stable in the numerical analyses without rock reinforcement with the assumed fracture properties according to Table 2-6. In all these cases, the maximum displacement remains small at the end of the excavation of the caverns, 2–3 cm. After a reduction of the fracture properties to realistic values for long term stability of no cohesion and a residual friction angle of 15° the caverns are still stable.

Results from 8 DFN realizations show that blocks along the excavation boundaries become unstable when the friction angle of the fractures is reduced to 5.7–8.7° with the in situ stresses according to Table 2-9. Even though only eight DFN realizations have been used, the length of the caverns (100 m) considered in the models and their large width makes it quite certain that the critical block configurations have been captured. Achieving these low friction angles in the fractures in a long-term perspective may occur locally in the rock mass. However, due to the geological characteristics of the rock mass surrounding the caverns, they will not occur in larger volumes that could affect the global stability.

The rigid block models show similar results compared to the calculations with the deformable block models. Blocks start to fall into the cavern at a reduced friction angle equal to 5.7°. The expansion of the loosening zone stops when the caverns are filled with blocks. The calculations also show that the zone of the loosened rock mass reaches a height of up to 34 m above the cavern roof. At this stage, the deformation at the rock surface is about 3.5 cm. However, it should be emphasized that the friction angle required to make this happen is unrealistically low. This model is therefore not realistic.

The results show that the pillar should remain overall stable after a reduction of the fracture properties to realistic values for long term stability of no cohesion and a residual friction angle of 15 degrees. Furthermore, the results show that overall stability should not be compromised even for the very low fracture friction angles (5.7°–8.7°) needed to make the excavation boundaries unstable. Locally, however, in the long term, a few boundary blocks may become loose and fall.

References

SKB's (Svensk Kärnbränslehantering AB) publications can be found at www.skb.se/publications. References to SKB's unpublished documents are listed separately at the end of the reference list. Unpublished documents will be submitted upon request to document@skb.se.

Barton N, 2002. Some new *Q*-value correlations to assist in site characterisation and tunnel design. International Jornal of Rock Mechanics and Mining Sciences 39, 185–216.

Barton N, Choubey V, 1977. The shear strength of rock joints in theory and practice. Rock Mechanics 10, 1–54.

Carlsson A, Christiansson R, 2007. Construction experiences from underground works at Forsmark. Compilation report. SKB R-07-10, Svensk Kärnbränslehantering AB.

Christiansson R, Bolvede P, 1987. Byggnadsgeologisk uppföljning. Slutrapport. SKB SFR 87-03, Svensk Kärnbränslehantering AB. (In Swedish.)

Glamheden R, Mærsk Hansen L, Fredriksson A, Bergqvist L, Markström I, Elfström M, 2007a. Mechanical modelling of the Singö deformation zone. Site descriptive modelling Forsmark stage 2.1. SKB R-07-06, Svensk Kärnbränslehantering AB.

Glamheden R, Fredriksson A, Röshoff K, Karlsson J, Hakami H, Christiansson R, 2007b. Rock mechanics Forsmark. Site descriptive modelling Forsmark stage 2.2. SKB R-07-31, Svensk Kärnbränslehantering AB.

Horn H M, Deere D U, 1962. Frictional characteristics of minerals. Géotechnique 12, 319–335.

Itasca, 2011. 3DEC – 3 Dimensional Distinct Element Code. Version 3DEC dp 4.20.123 64 bit. Minneapolis, MN: Itasca Consulting Group, Inc.

SKB, 2001. Project SAFE. Scenario and system analysis. SKB R-01-13, Svensk Kärnbränslehantering AB.

SKB, 2002. Forsmark – site descriptive model version 0. SKB R-02-32, Svensk Kärnbränslehantering AB.

SKB, 2008. Safety analysis SFR 1. Long-term safety. SKB R-08-130, Svensk Kärnbränslehantering AB.

SKB, 2014. Safety analysis for SFR. Long-term safety. Main report for the safety assessment SR-PSU. SKB TR-14-01, Svensk Kärnbränslehantering AB.

Unpublished documents

SKBdoc id, version	Title	Issuer, year
1237025 ver 2.0	PM angående långtidsstabilitet hos bergrum och tunnlar i SFR (In Swedish.)	SKB, 2010

Appendix 1

Sensitivity to in situ stress

To investigate the sensitivity to in situ stress a simulation with isotropic (hydrostatic) stress was run with the DFN generated with the random seed number 105 (Figure 4-6).

The stress magnitude used in this simulation run follows the following equations:

$\sigma_H = 0.027z$ MPa

$\sigma_h = 0.027z$ MPa

$\sigma_v = 0.027z$ MPa

where z is depth from the surface.

The stress orientation is the same as in the previous cases.

The results of these simulations (Figure A-1 to A-5) indicate that the caverns are stable after excavation without reinforcement and become unstable (blocks begin to fall) when the fracture friction angle is reduced to 18.23°.

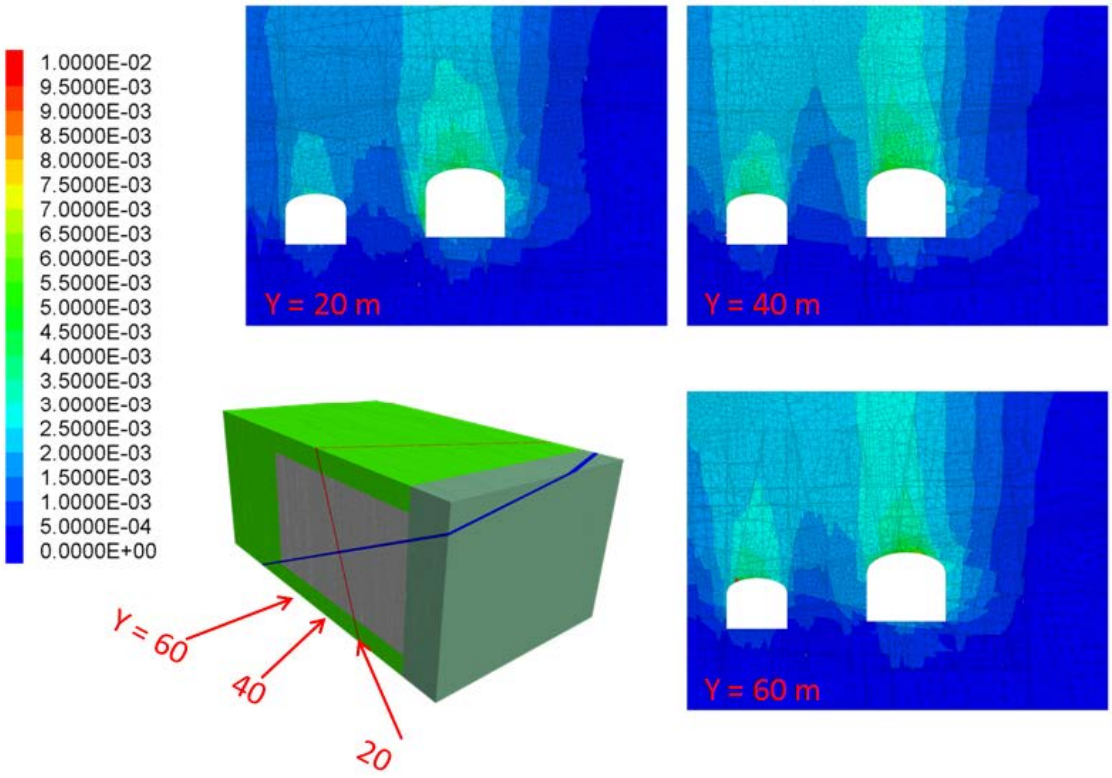

Figure A1-1. *Vertical cross-section contour plots of the displacements (in m) after excavation for case 105 (Figure 4-6) – hydrostatic stress. Cross section perpendicular to both caverns at Y = 20 m, Y = 40 m and Y = 60 m.*

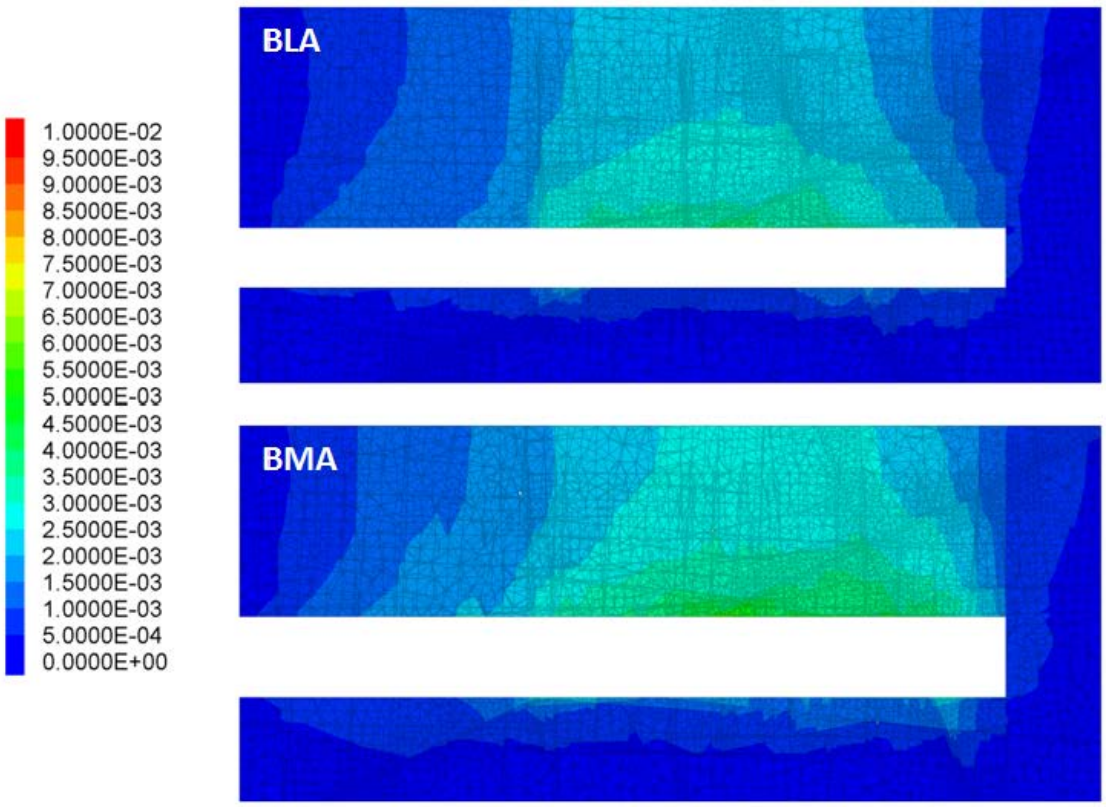

Figure A1-2. *Vertical cross-section contour plots of the displacements (in m) after excavation for case 105 (Figure 4-6) – hydrostatic stress. Two cross sections parallel to the caverns axis cutting through the middle of BLA cavern (upper) and BMA cavern (lower).*

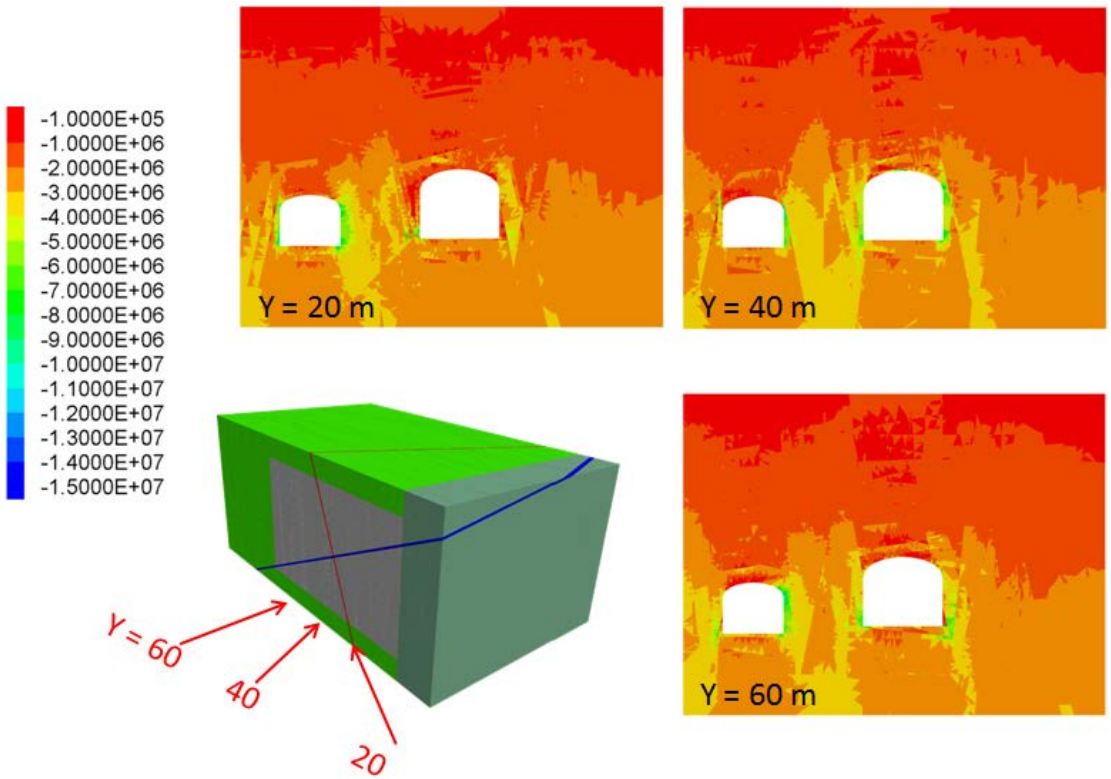

Figure A1-3. *Vertical cross-section contour plots of the maximum principal stress magnitude (in Pa) after excavation for case 105 (Figure 4-6) – hydrostatic stress. Cross section perpendicular to both caverns at Y = 20 m, Y = 40 m and Y = 60 m.*

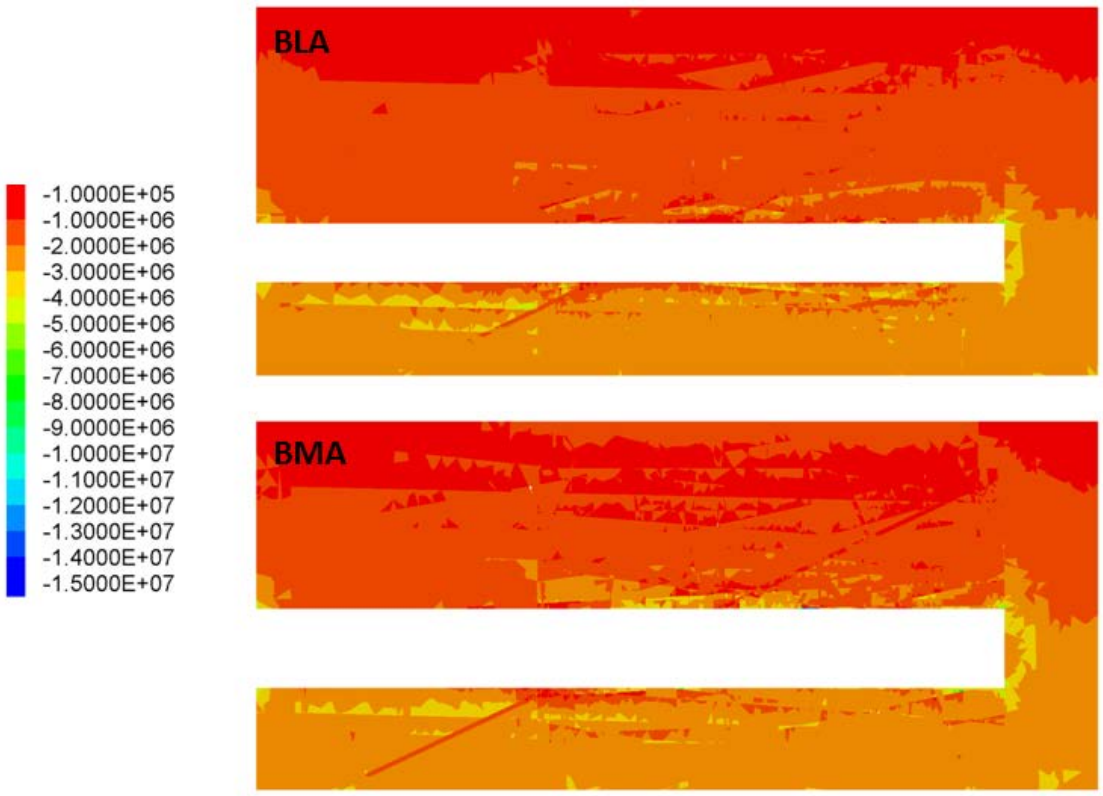

Figure A1-4. *Vertical cross-section contour plots of the maximum principal stress magnitude (in Pa) after excavation for case 105 (Figure 4-6) – hydrostatic stress. Two cross sections parallel to the caverns axis cutting through the middle of BLA cavern (upper) and BMA cavern (lower).*

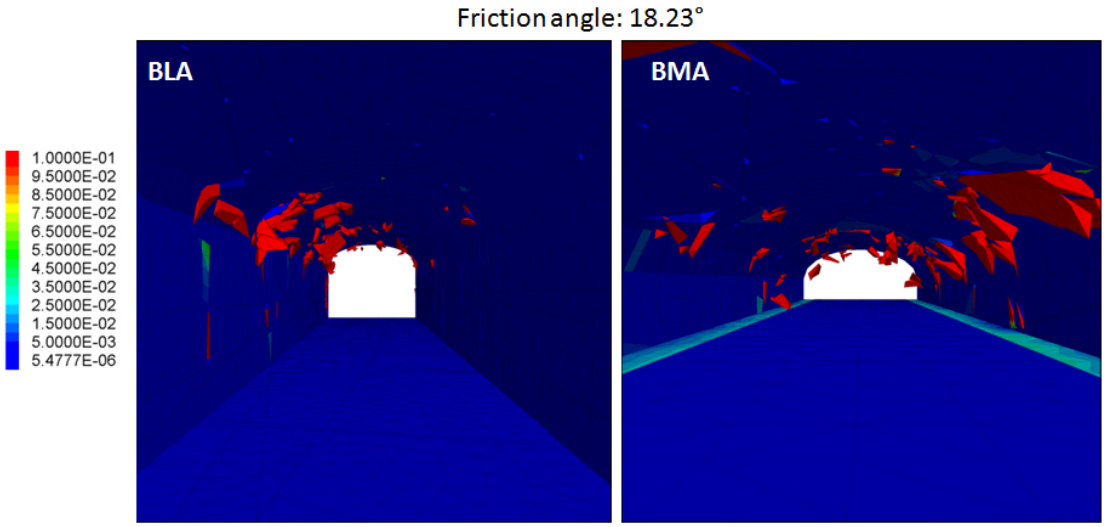

Figure A1-5. *3 dimensional view of the caverns with displacement contours (in m) once the critical fracture friction angle has been reached for case 105 (Figure 4-6) – hydrostatic stress.*